STUDIES OF TWO-DIMENSIONAL ATOMIC HYDROGEN GAS WITH ELECTRON-SPIN RESONANCE

by

Jarno Järvinen
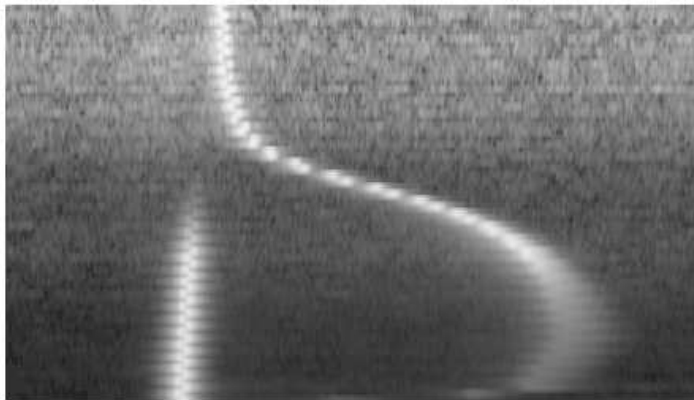
From the Wihuri Physical Laboratory
Department of Physics
University of Turku
Turku, Finland
and
National Graduate School in Materials Physics
Helsinki, Finland

Supervised by

Docent Simo Jaakkola and Dr. Sergei Vasiliev, PhD
Wihuri Physical Laboratory
Department of Physics
University of Turku
Turku, Finland

Reviewed by

Prof. Matti Krusius   Prof. Henrik Kunttu
Low Temperature Laboratory   Nanoscience Center
Helsinki University of Technology   University of Jyväskylä
Finland   Finland

Opponent

Prof. Michael E. Hayden
Department of Physics
Simon Fraser University
Burnaby, B. C.
Canada

Acknowledgements

Turku, March 2006

Jarno Järvinen

Abstract

In this thesis experiments are described where spin-polarized atomic hydrogen gas was studied in the 100 mK temperature range with continuous-wave electron-spin resonance (ESR) at 129 GHz. The chief interest of this work is two-dimensional (2D) H gas adsorbed on the surface of superfluid ^{4}He. Interatomic interactions and a possibility to observe superfluidity in this 2D system were studied. For the experiments a sensitive heterodyne ESR spectrometer was constructed with its main mm-wave components being installed into a dilution refrigerator. ESR signals from both bulk (3D) hydrogen and surface-adsorbed atoms were detected using a semi-confocal Fabry-Perot resonator. To measure the 2D H density we utilized the shift of the surface ESR line with respect to the bulk line position due to magnetic dipole interactions between the adsorbed H atoms.

The 2D gas was compressed thermally on a small "cold spot" maintained at temperatures ranging from 50 mK to 150 mK. The ESR signal from the surface atoms was found to be sensitive to the ESR excitation power such that higher powers gave rise to a nonlinear response of the signal thus causing difficulties in the detection of the surface atoms at low temperatures. The line shape of the 2D gas spectra was sensitive also to the inhomogeneous density profile across the cold spot. Origins of the observed linewidth of the surface atoms are discussed, too.

Simultaneous measurement of the time evolutions of the bulk and surface atomic densities and of the recombination energy enabled us to make the first direct determination of the surface three-body rate constant L_3^s. Being about an order of magnitude smaller than numerous results reported earlier, the value $L_3^s = 2(1) \times 10^{-25}$ cm^{4}s^{-1} obtained in this work considerably decreases the discrepancy between the experiments and the theory.

The maximum surface density reached for H in this work was 5.5×10^{12} cm^{-2} corresponding to the 2D phase-space density of 1.6. Information extracted from experiments in different conditions allowed us to learn of limiting factors to thermal compression. One of them was an inadequate escape of highly excited molecules from the cold spot which results in a significant overheating of the surface gas. Possibilities to boost the surface density further even up to the onset of 2D superfluidity in thermally compressed atomic hydrogen are considered.

Preface

This thesis is based on a series of experiments carried out during the years 2001-2005 and on seven original papers listed below. The introductory part of the thesis contains also new unpublished data.

P1.   S. Vasilyev, J. Järvinen, A. I. Safonov, A. A. Kharitonov, I. I. Lukashevich, and S. Jaakkola, *Electron-spin-resonance instability in two-dimensional atomic hydrogen gas,* Physical Review Letters **89**, 153002 (2002).

P2.   S. Vasilyev, J. Järvinen, A. I. Safonov, and S. Jaakkola, *Thermal compression of two-dimensional atomic hydrogen gas,* Physical Review A **69**, 023610 (2004).

P3.   S. Vasilyev, J. Järvinen, A. I. Safonov, and S. Jaakkola, *Electron-spin resonance in quantum degenerate 2D atomic hydrogen gas,* Physica B **329-333**, 19 (2003).

P4.   S. Vasilyev, J. Järvinen, E. Tjukanoff, A. A. Kharitonov, and S. Jaakkola, *Cryogenic 2 mm wave electron spin resonance spectrometer with application to atomic hydrogen gas below 100 mK*, Review of Scientific Instruments **75**, 94 (2004).

P5.   T. Peltonen, E. Tjukanoff, J. Järvinen, and S. A. Vasilyev, *A Fabry-Perot cavity for millimeter wave ESR detection of hydrogen atoms at low temperatures*, Proceedings of 3rd ESA Workshop on Millimetre Wave Technology and Applications: Antennas, Circuits and Systems, Eds. J. Mallat, A. Räisänen, J. Tuovinen, 21-23 May 2003, Espoo, Finland, ESA WPP-212, 2003, p. 447.

P6.   J. Järvinen, J. Ahokas, S. Jaakkola, and S. Vasilyev, *Three-body recombination in two-dimensional atomic hydrogen gas*, Physical Review A, **72,** 052713 (2005).

P7.   Jarno Järvinen and Sergei Vasilyev, *Atomic hydrogen gas at the surface of superfluid helium*, Journal of Physics: Conference Series **19,** 186 (2005)

My contribution to the papers is described in the following list:

P1.   I took part in the measurements and data analysis.

P2.   I took part in the measurements, data analysis and writing the paper.

P3.   I made the measurements.

P4.   I participated in the design, assembly, testing and tuning of the spectrometer and also wrote part of the paper.

P5.   I made the numerical FEM calculations of the resonator model.

P6.   I ran the measurements, analyzed the results and wrote most of the paper.

P7.   I wrote the paper.

Contents

1 Introduction

1.1 Background

Our world is spatially three-dimensional (3D). In some cases the motion of particles is however tightly restricted to two or even one dimension. A gas adsorbed on the walls of a container presents an example of a two-dimensional (2D) system. One may ask whether and how widely the low-dimensional systems differ from the 3D ones in their physical behaviour? The somewhat surprising answer is that usually physics in 2D is less straightforward than in 3D. Quite a general example is the wave equation in 2D space where the Huygens principle does not hold and the propagation of the wave is different from that in 3D. An incident creating a sharp wave front in 2D space is followed by a slowly decaying tail [1] which can be seen for example in waves travelling on the surface of water. Good examples of the effect of dimensionality are also the integer and fractional quantum Hall effects originating from the discrete quantization of the Landau levels of conduction electrons in solids having 2D geometry.

Especially after the first observations in 1995 of Bose-Einstein condensation (BEC) in clouds of trapped alkali atoms [2, 3] there has been interest to observe this phenomenon also in 2D quantum gases. BEC is a quantum statistical transition in phase space where the population of the ground state of a boson system becomes macroscopic below a critical temperature T_c. (A boson is composed of an even number of fermions thus having an integer spin and obeying Bose statistic). From the quantum field theory point of view BEC is a manifestation of spontaneous breaking of a continuous phase symmetry at T_c. However, in 2D space this is not possible for a uniform system at a finite temperature, as proved by the Mermin-Wagner-Hohenberg theorem [4, 5, 6]. Superfluidity is in turn regarded as a manifestation of BEC, but in 2D the onset of superfluidity is a topological phase transition, the so-called Berezinskii-Kosterlitz-Thouless (BKT) transition [7, 8], which is different from BEC [9]. The BKT transition has been observed in thin films of liquid ^{4}He [10] which are strongly interacting boson systems. The BKT theory predicts the formation of superfluidity at $\sigma\Lambda^2 = 4$ due to the binding of vortices into pairs at T_c [8], but it has never been observed in any weakly interacting system. Here σ is the 2D density of atoms and Λ the thermal de Broglie wavelength. Above T_c the vortex pairs are free to move and prevent the superfluid flow.

The theory of Popov [11] introduced the concept of quasi-condensate (QC) where there are no density fluctuations but phase fluctuates spatially. A QC can be visualized being divided into domains or "blocks" which are smaller than the phase coherence length but much larger than the healing length. There is a true condensate inside each block but there is no phase correlation between the blocks [12]. Popov's theory is further developed in refs.

[13, 14, 15] and Monte Carlo simulations of 2D Bose gas can be found in refs. [16, 17]. A view emerges that below the BKT transition temperature the 2D superfluid is characterized by the presence of a QC, but it is unclear what is the relation between the BKT and QC (or BEC) transitions.

The unique advantage of hydrogen in attaining the conditions of BEC was believed to be the light atomic mass, which implies a high BEC temperature and prevents the sample from becoming liquid or solid before quantum effects can take place. This advantage could not easily overcome two disadvantages of H atoms, their recombination into H_2 molecules and the exceptionally small scattering cross-section. The latter property makes thermalization of evaporation-cooled atoms in magnetic traps by H-H collisions tedious. Actually after the first stabilization of spin-polarized atomic hydrogen (H↓) in 1979 [18] it took almost two decades until the first hydrogen BEC was achieved by a research team at MIT [19] who used standard cryogenic and evaporative cooling of trapped H↑ down to about 50 μK. At the same time interest was also directed towards 2D H↓ adsorbed on the surface of liquid helium and experimental evidence of a quasi-condensate in this system was obtained at Turku in 1997 [20]. Three-dimensional alkali atom condensates have also been "squeezed" to dimensional crossover in 1D and 2D traps including optical lattices, [21] magnetic traps [22] and evanescent wave traps [23]. Phase fluctuations have already been seen in quasi-2D (and 3D) alkali condensates [24, 25], but the BKT transition has not been observed in them yet.

In the Turku experiment the formation of a quasi-condensate in H↓ was observed as a drastic reduction of inelastic three-body collisions when the 2D phase-space density exceeded $\sigma \Lambda^2 \approx 3$ [20]. The sample was compressed at the surface of superfluid ^{4}He film with the help of a strong magnetic field gradient. Due to distortions of spectra caused by the very inhomogeneous field it was not possible to combine magnetic compression with magnetic resonance spectroscopy of surface atoms. Therefore, the method of thermal compression, first applied to H↓ by T. Mizusaki and coworkers at Kyoto University, [26] was pursued in the work described in this thesis.

Interactions between H↓ atoms in 2D and with the helium film are other interesting issues. The exchange interaction is known to be very important in elastic collisions of atoms. It leads to a shift and broadening of the spectral lines in masers, known as the "clock" or "cold collision" frequency shift. Recently similar effects were studied in Bose-condensed and normal clouds of alkali vapours with magnetic resonance spectroscopy [27, 28, 29]. But for 2D H↓ gas the clock shift was found [30] to be negligibly small compared to dipolar shifts, caused by much weaker magnetic interactions. It is not known yet whether this difference is caused by the reduced dimensionality or by the much larger magnetic field used.

The introductory part of the thesis is organized as follows: Chapter 1 includes, in addition to this general introduction, short review of interatomic interactions, recombination, and properties of 2D and 3D atomic hydrogen gas. Details of electron-spin resonance are also described. Chapter 2 covers the experimental details of the work. Description of different parts of the experimental apparatus and of the measurement procedures are considered. In chapter 3 electron-spin resonance line shapes and temperature of the surface adsorbed atoms are discussed. Limiting factors preventing to increase 2D H↓ density with thermal compression are estimated at the end of the chapter. The conclusions of this work are summarized in chapter 4.

1.2 Properties of H gas in 2D and 3D

1.2.1 Atomic states and interatomic potentials

Provided the density of a many-body system formed by the lightest elements is sufficiently high, quantum effects will create detectable changes in the macroscopic properties of the system already at relatively high temperatures. Under its own vapour pressure ^{4}He does not solidify but liquefies at 4.2 K. Except for liquid ^{3}He, which is however composed of fermions, ^{4}He atoms form the only bulk liquid known to undergo a transition to a superfluid state at 2.17 K. Unfortunately the relative strong interatomic interactions in liquid helium effectively mask the quantum effects and complicate the theoretical analysis of the system.

Being even lighter than He, atomic hydrogen is expected to exhibit more pronounced quantum effects. It turns out in fact that if H atoms interact via the triplet (or symmetric, denoted as $^3\Sigma_u^+$) potential [31, 32], the state with parallel electron spins, then the zero-point energy overwhelms the very weak minimum of the otherwise repulsive triplet potential. This makes it possible that spin-polarized hydrogen remains gaseous down to the absolute zero temperature [33]. The attractive singlet (or antisymmetric, denoted as $^1\Sigma_g^+$) potential [31, 32] of antiparallel electron spins supports altogether 301 rotational and vibrational bound states including the stable H_2 molecular ground state as much as 52000 K$\times k_B$ [34, 35] below the continuum. So it is the strong singlet interaction that tends to (re)combine H atoms into H_2 molecules which then solidify already at 14 K.

An external magnetic field $B = |\mathbf{B}|$ fixes a preferential orientation for the spins. The Hamiltonian for a single hydrogen atom in a magnetic field is

$$\hat{H} = g_e \mu_b \mathbf{S} \cdot \mathbf{B} + g_n \mu_n \mathbf{I} \cdot \mathbf{B} + a_h \mathbf{S} \cdot \mathbf{I}, \tag{1}$$

where g_e and g_n are electron and nuclear g-factors, respectively, μ_b and μ_n are the Bohr and nuclear magnetons and a_h is the hyperfine interaction constant. The Hamiltonian (1) has four energy eigenstates. These hyperfine states, often labelled from a to d with increasing
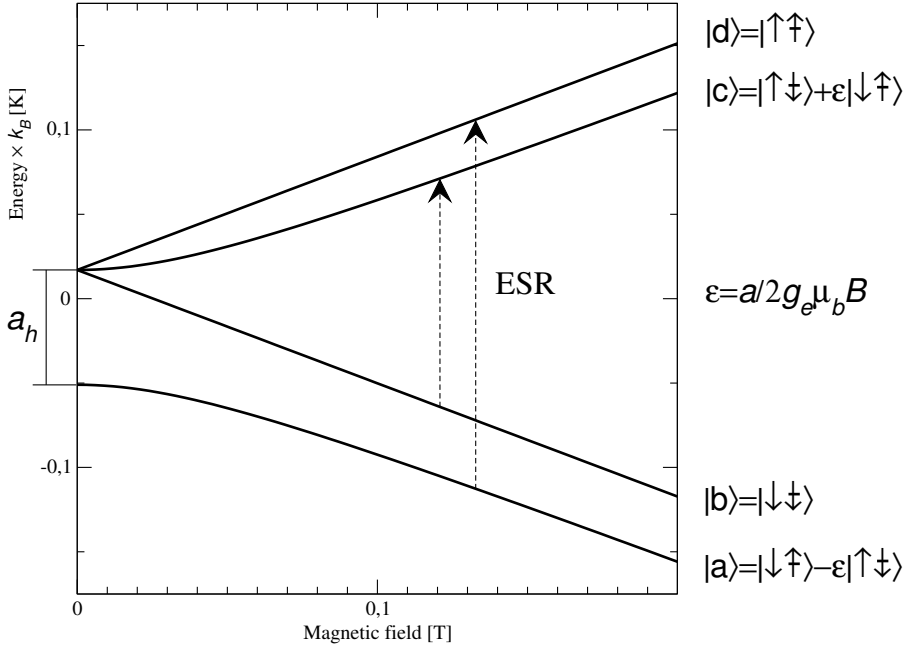
Figure 1: Breit-Rabi diagram of hydrogen hyperfine states and transversal ESR transitions.

energy, are illustrated in fig. 1. Depending on the electron-spin polarization, atoms in the states a and b (H $\downarrow$) are attracted to and in c and d (H $\uparrow$) repelled from an increasing magnetic field. This makes it possible to accumulate an electron spin-polarized H $\downarrow$ sample, e.g., in the center of a solenoid. Atoms in the same state interact chiefly through the triplet interaction making them quite stable against recombination. Due to the hyperfine interaction the states a and c are mixed containing, in high magnetic field, the fraction $\varepsilon \approx a_h/2g_e\mu_b B$ of the opposite electron spin state, whereas b and d are "doubly polarized" or "pure" Zeeman states, respectively (H$\downarrow\Downarrow$ and H$\uparrow\Uparrow$). Interactions $a - b$ and $a - a$ or $c - d$ and $c - c$ contain a fraction $\propto \varepsilon$ of singlet character which leads with finite the probability to exchange recombination [36, 37]. This mechanism is not operative in doubly polarized hydrogen.

In addition to Coulomb, exchange, and Zeeman interactions there is also an interaction between the magnetic moments of H atoms. It is about six orders of magnitude weaker than the exchange interaction and is therefore usually neglected in calculations. However, in certain cases these dipolar interactions can cause notable effects and one of them is the dipolar recombination [36, 38] which operates even in the doubly polarized gas. The dipolar interactions are also responsible for the frequency shift between the ESR lines originating from bulk H$\downarrow$ and surface-adsorbed H$\downarrow$. The average dipolar shift of the bulk H$\downarrow$ line is negligible in our experimental density range but this is not the case for 2D H$\downarrow$. The surface

line shift, which is linear in density and depends on the orientation of the magnetic field, is given by the relation [30]

$$B_d = -\alpha_d P_2(\cos\theta)\sigma, \tag{2}$$

where α_d is a proportionality constant, θ is the angle between **B** and the surface normal and P_2 is a Legendre polynomial. The dipolar shift was first observed by Reynolds *et al.* [39] and Shinkoda *et al.* [30], although their experiments suffered from too high ESR excitation power causing nonlinear effects in the 2D line shape. In this work the value $\alpha_d = 1.0(1) \times 10^{-12}$ G cm^2 [P1, P7] has been measured up to the surface density of $\sigma \approx 5 \times 10^{12}$ cm^{-2}.

1.2.2 Atomic hydrogen adsorbed on liquid helium

The surface of superfluid ^{4}He offers unique properties for creating samples of 2D H↓ gas. First, the H-He van der Waals interaction is one of the weakest in its class. The effective interaction potential perpendicular to the He surface was calculated by Guyer and Miller [40] and Mantz and Edwards [41] who showed that there is only one bound energy eigenvalue E_a for H on the ^{4}He surface. Trapping of H atoms into this bound state will create a 2D gas, in which the average distance of the atoms from the surface and the perpendicular delocalization length l_d are both about 0.6 nm. Secondly, the surface of ^{4}He is completely uniform. Compared to solids it does not have any periodicity or roughness to disturb the free particle-like motion of the H atoms along the surface. At temperatures of about 300 mK or less ^{4}He vapour is already in the high-vacuum pressure range.

If one takes into account the elementary surface excitations, called ripplons, the ^{4}He surface is not completely flat. The amplitude of these quantized capillary waves is only about 0.1 nm [42, 43] and the wavelength is much longer than the range of the interatomic interaction [9]. Therefore, ripplons do not influence the H-H scattering. However, in the cooling of the surface hydrogen the ripplons do play an important role (see below). At low surface temperatures T_σ the surface density σ of H atoms increases exponentially with decreasing T_σ. This will increase the number of interatomic collisions and recombination rate. It is therefore necessary to have the binding of H atoms to the surface as weak as possible thus extending the sample lifetime and reducing the recombination heating of the sample. An extreme example of 2D trapping is the magnetic and optical wall-free confinement applied to alkali atoms [22, 23, 44, 45]. However, for H the optical trapping is very difficult to realize and with the magnetic method it is difficult to reach the 2D confinement offered by liquid helium surfaces. Anyhow, we may say that the H-He interaction gives a nice possibility to create a genuine 2D quantum gas of H atoms.

The 2D H gas on a free liquid ^{4}He surface is in dynamical equilibrium with the bulk

gas. Continuous exchange of atoms between the bulk and surface-adsorbed phases occurs at a rate depending exponentially on temperature. A relation between the densities of the surface and bulk gases, respectively σ and n, in thermal equilibrium is found by equating the chemical potentials of the two phases. In the high temperature and low density limit this will lead to the well-known classical equation for the adsorption of a Boltzmann gas:

$$\sigma = \left(\frac{T_b}{T_\sigma} \right)^{\frac{3}{2}} n\Lambda \exp\left(\frac{E_a}{k_B T_\sigma} \right), \tag{3}$$

where T_b is the bulk gas temperature and T_σ is the surface gas temperature. The prefactor $(T_b/T_\sigma)^{3/2}$ takes into account the possible temperature difference between the bulk and surface gases [46]. Alternatively, σ can be expressed by equating the adsorbing and desorbing H atom fluxes. The surface residence time τ_r is exponentially proportional to the ratio $E_a/k_B T_\sigma$. Taking quantum correlation effects and the H-H interaction energy into account τ_r is given [46] by the relation

$$\frac{1}{\tau_r} = \frac{k_B T_\sigma s}{2\pi\hbar} \cdot \frac{1 - \exp(-\sigma\Lambda^2)}{\sigma\Lambda^2} \exp\left(\frac{-E_a + g_2 U_2 \sigma}{k_B T_\sigma} \right). \tag{4}$$

Here U_2 stands for the H-H mean field interaction energy, g_2 is a two-body correlation function and $s \approx 0.33 \times T_\sigma$ K^{-1} [47, 48] is the sticking probability of H atoms to the ^{4}He surface. For non-degenerate identical bosons $g_2 = 2$ and for non-identical or degenerate bosons $g_2 = 1$. For low densities of $\sigma < 10^{13}$ cm^{-2} and temperatures of about 100 mK $\tau_r \approx 1.4$ ms. The exponential growth of σ, proportional to $E_a/k_B T_\sigma$, is essential for the thermal compression method used in this work to compress 2D H↓ gas. In an ideal case a compression factor of about 100 is achieved when the temperature is lowered, e.g., from 100 mK to 70 mK.

Eq. (3) also yields T_σ provided E_a, σ and, n are known. The adsorption energy will not be affected by the solid substrate beneath the liquid ^{4}He layer unless the latter is thinner than about 20 monolayers [49] (the saturated film is 110 monolayers). There is some scatter in the experimental values of E_a for H on liquid ^{4}He ranging from 0.9 K to 1.15 K [30, 50, 51, 52, 53]. The values extracted from fits to decay rate equations, including multiple fitting parameters, are considered to be less accurate than those obtained from magnetic resonance experiments. The experimental results obtained in the present work support the value $E_a/k_B = 1.14(1)$ K [P1, P2].

Adsorbed hydrogen atoms are in thermal equilibrium with the ripplon system of the superfluid helium surface. This is because the momentum of an adsorbed atom is relaxed in a time τ_p due to emission and scattering of ripplons. At 100 mK the value $\tau_p = 3 \times 10^{-8}$ s [54] is much shorter than the surface residence time τ_r, ensuring thermal equilibrium

between H and ripplons. The ripplons are in weak thermal contact with the phonon system of the liquid, from which heat is eventually transferred to the sample cell body. The large thermal resistance between the ripplons and the phonons of the ^{4}He film creates a bottleneck in the cooling of the 2D H gas. For the phonon system at a temperature T_{ph} the maximum cooling power has been calculated to be

$$P_{rp} = G_{rp}(T_\sigma^{20/3} - T_{ph}^{20/3}),\tag{5}$$

where $G_{rp} = 0.84$ Wcm^{-2}K$^{20/3}$ is the heat conductance of the ripplon-phonon contact [55]. The cooling power is strongly temperature dependent and G_{rp} is smaller than the Kapitza conductance across, e.g., metal/^{4}He interfaces below 100 mK [56].

The properties of a weakly interacting 2D Bose gas like H↓ are characterized by four length scales. First there is the 3D s-wave scattering length a_{3D} which defines the 3D mean-field interaction energy $U_3 = 4\pi\hbar^2 a_{3D}/m$ between the particles of mass m at low temperatures. The second length is the effective range of interaction R_e, which is generally not equal to a_{3D} [12, 57]. The third characteristic distance is the de Broglie wavelength Λ. When $\Lambda \gg R_e$ the system is in the s-wave scattering limit. The fourth length scale is the delocalization length $l_d = \sqrt{\hbar^2/mE_a}$ [12] in the surface-normal direction. In a truly 2D system $l_d/a_{3D} \lesssim 1$ and particle scattering is strongly affected by the confinement making the interaction always repulsive [58]. Scattering is three-dimensional if $l_d/a_{3D} \gtrsim 10$ [57]. The intermediate region may be called a quasi-2D region where collisions can be described by purely 2D scattering but the interaction strength depends on l_d [58]. The condition for weakly interacting gas in the quasi-2D case is $|a| \ll l_d$ [12]. For H on ^{4}He surface $a_{3D} \approx 0.07$ nm [59, and references therein] and $l_d/a_{3D} \approx 10$. This shows that 2D H is a weakly interacting system and that short-range interactions are still three-dimensional. This is also seen in the 2D mean field interaction energy which in the quasi-2D range is given by [12]

$$U_2 = \frac{4\pi\hbar^2}{m} \frac{1}{\sqrt{2\pi}l_d/a_{3D} + \ln(0.291E_a/E_k)} \approx \frac{2\sqrt{2\pi}\hbar^2}{m} \frac{a_{3D}}{l_d}\tag{6}$$

where E_k is the thermal energy of motion in the plane. For 2D H at 100 mK $E_a/E_k \approx 11.4$ and the logarithmic term in eq. (6) is only about 5 % which shows that the scattering is essentially 3D as said above. Eq. (6) gives $U_2/k_B \approx 3 \times 10^{-15}$ Kcm^2 in agreement with refs. [43, 60]. It is interesting to note that if $a_{3D} < 0$ the sign of U_2 could be changed by modifying l_d [61].

The mean field interaction between atoms in different spin states is known to shift the radio-frequency resonance lines [28, 27]. This clock or cold collision frequency shift is caused by the differences of the mean field energy (eq. (6)) between different spin

states. The resonance frequency is also shifted differently for condensed and non-condensed bosons [28]. If the clock shift is larger than the resonance linewidth it can be used as an indicator of the the quasi-condensation. For 2D H↓↕ the cold collision frequency shift calculated from eq. (6) is about an order of magnitude larger than the dipolar shift [P7] given by eq. (2). The observed shift is smaller than the calculated one. The clock shift is isotropic and shifts the line towards higher frequencies, the direction being the same as for the dipolar shift on the plane perpendicular to the polarizing field. Using this information and the data of ref. [30] we may conclude that the clock shift is at most 0.4 times the dipolar shift given by eq. (2).

1.2.3 Recombination and relaxation

The stability of H↓ is determined by the rate of recombination of atoms into H_2 molecules in both bulk and surface phases. Numerous experimental and theoretical studies have been devoted to the decay kinetics of H↓ [34, 38, 51, 53]. Recombination and the large amount of energy released in it (4.48 eV per event) tend to prevent the attainment of high enough densities at low enough temperatures needed for the occurrence of quantum degeneracy. On the other hand, valuable information on the intrinsic processes of the gas can be obtained by monitoring the density decay of the H↓ sample and as a matter of fact this has been a very fruitful method of studying H↓. At densities $n \lesssim 10^{16}$ cm^{-3} and temperatures ≤ 200 mK bulk recombination is negligible and only surface recombination is significant. This is because conservation of momentum and energy in all recombination events requires at least three participating bodies. According to our knowledge no detailed description of H recombination exists that would take into account the dynamic properties of the He surface. If one simply assumes that there is no energy exchange between the colliding pair and the surface, the center of mass momentum along the surface is conserved and recombination can only take place if the molecule is desorbed at the same time [34].

When the gas is spin-polarized, recombination kinetics is considerably simplified and only two recombination channels are important. These are surface two-body exchange recombination and three-body dipolar recombination. The former occurs only if the colliding H atoms interact through the singlet potential. This implies that only $a-a$ and $a-b$ (see fig. 1) collisions can induce exchange recombination and the rate of this process decreases with increasing magnetic field as $\varepsilon^2 \propto B^{-2}$. In a pure b-state (H↓↕) sample there is no exchange recombination, and the three-body dipolar process is the main source of recombination but only at high densities. The dipolar interaction is important when the initial three particle state has no singlet character. When a pair of atoms collide in the dipolar field of a third atom the variations of the magnetic field induce a singlet component into the interaction of the pair [36, 38]. This may lead to recombination and, depending on whether the third atom

changes or does not change its electron-spin orientation, the event is called single- or double spin-flip process [34, 62]. In the latter the third atom will recombine in a collision with a fourth atom. In experiments we measure the total loss rate of atoms and cannot distinguish between the single and double spin-flip mechanisms in H↓⇂.

In addition to the recombination, decay of H↓ is influenced by the nuclear relaxation rate between a- and b-states. Two surface relaxation processes can be met in experiments: impurity induced one-body relaxation and intrinsic two-body relaxation [34]. The former is a consequence of small spatial fluctuations in the magnetic field caused by magnetic materials e.g. small grains of iron embedded in the walls during machining. The magnetic moments of the atoms can also induce eddy currents in a highly conducting surface leading to the relaxation. Impurity relaxation can be reduced to a negligible level by careful fabrication of the cell from nonmagnetic materials and by covering the cell walls with a dielectric layer. Such a layer can be grown from solid H_2 by keeping the hydrogen filling flux on continuously for a long enough time. The two-body surface relaxation process is anisotropic such that its rate is zero for a surface oriented perpendicular to the polarizing field [34]. In the sample cells used in the present work there are no walls with high H↓ surface density parallel to the polarizing field and the two-body relaxation was found to be of no importance.

The recombination kinetics is described by rate equations which are coupled first-order differential equations. The rate constant of one-body relaxation is usually marked as G, the two-body recombination as K, and the three-body recombination loss rate constant as L_3. For H↓ the equations are

$$
\begin{aligned}
\dot{a} &= -G^e(a-b) - K^e_{ab}ab - 2K^e_{aa}a^2 \\
\dot{b} &= G^e(a-b) - K^e_{ab}ab - L^e_3 b^3
\end{aligned}
\quad ,
\tag{7}
$$

where a and b are the partial bulk densities of the corresponding hyperfine states, and we have neglected three-body processes which include the a-state. Here, the superscript e stands for effective bulk rate constants [34] used to transform the intrinsic surface rates (superscript s) to the effective bulk ones through the adsorption isotherm eq. (3). The effective rate constants are given by

$$
\begin{aligned}
G^e &= \frac{A_h}{V_h}\Lambda(\frac{T_b}{T_\sigma})^{3/2}G^s e^{E_a/k_B T_\sigma} \\
K^e_{ij} &= \frac{A_h}{V_h}\Lambda^2(\frac{T_b}{T_\sigma})^3 K^s_{ij}e^{2E_a/k_B T_\sigma} \\
L^e_3 &= \frac{A_h}{V_h}\Lambda^3(\frac{T_b}{T_\sigma})^{9/2}L^s_3 e^{3E_a/k_B T_\sigma},
\end{aligned}
\tag{8}
$$

where A_h and V_h are the area and volume of the sample cell. Values of the surface recombination rate constants are given in table 1. Due to the large exponential factors surface

Table 1: Experimental values of two- and three-body surface recombination rate constants of H↓ on ^{4}He at $B \geq 4$ T and $T \leq 250$ mK.

Coefficient	Value	Units	Reference
K_{aa}^s	$0.4(1) \times 10^{-7}\sqrt{T}/B^2$	$\mathrm{cm^2 s^{-1} K^{-1/2} T^2}$	[53, 34]
K_{ab}^s	$0.4(1) \times 10^{-7}T^{3/2}/B^2$	$\mathrm{cm^2 s^{-1} K^{-3/2} T^2}$	[53]
L_3^s	$2.0(7) \times 10^{-25}$	$\mathrm{cm^4 s^{-1}}$	[P6]*

* Value measured in a field of 4.6 T

recombination is effectively reduced by increasing the surface temperature. In thermal equilibrium at $T \gg 40$ mK the a-state population should be nearly equal to that of the b-state. However, if G^e is small, the a-state density is exhausted in the $a-a$ and $a-b$ recombinations [34], and the sample evolves from H↓ to H↓↕ on a timescale of $(K_{aa}^e a)^{-1}$, which in the present work is about 100 s at 170 mK. Then, recombination of H↓↕ is possible only by $a-b$ surface relaxation and the three-body process. If the surface density is small enough, the three-body term can be neglected and the density decay is exponential.

A recombination event on the surface releases a large amount of energy. However, liquid helium does not absorb all the recombination energy at once and only a fraction $f \lesssim 2$ % is released directly at the recombination site [63, 64, 65]. The rest is evenly distributed on the sample cell walls by excited H_2^* molecules relaxing towards their ground state. The idea of local compression takes advantage of such a spreading of the recombination heat. Recombination products carry away most of the heat, provided they can freely escape from the compression region. Cooling only a small cold spot (CS) on the wall of the sample cell to a low temperature makes it possible to compress the 2D H gas locally. In such a case the total heat absorbed by the cold spot is strongly reduced. In addition to the fraction f of three-body recombination energy there are two other important sources of heat. One is associated with the one-body relaxation on the sample cell walls, and the second is due to the thermal accommodation of the bulk gas. In fig. 2 the contributions of different heating processes at the experimental conditions of this work are presented as a function of the cold spot temperature T_σ. The surface density is fixed to 3×10^{12} cm^{-2} and the bulk density is calculated from eq. (3). To avoid large thermal accommodation heating it is better to work at $n < 10^{16}$ cm^{-3}. Then, the value of σ is set by the balance between the direct three-body recombination heating and cooling of the cold spot (eq. (5)).

Three-body recombination can be also used as a probe of the appearance of quantum degeneracy. The probability of three-body recombination is proportional to the three-particle correlation function. In a condensate the density fluctuations are suppressed and the three-body correlation function decreases by a factor of 3! [66, 67]. Whether this applies also
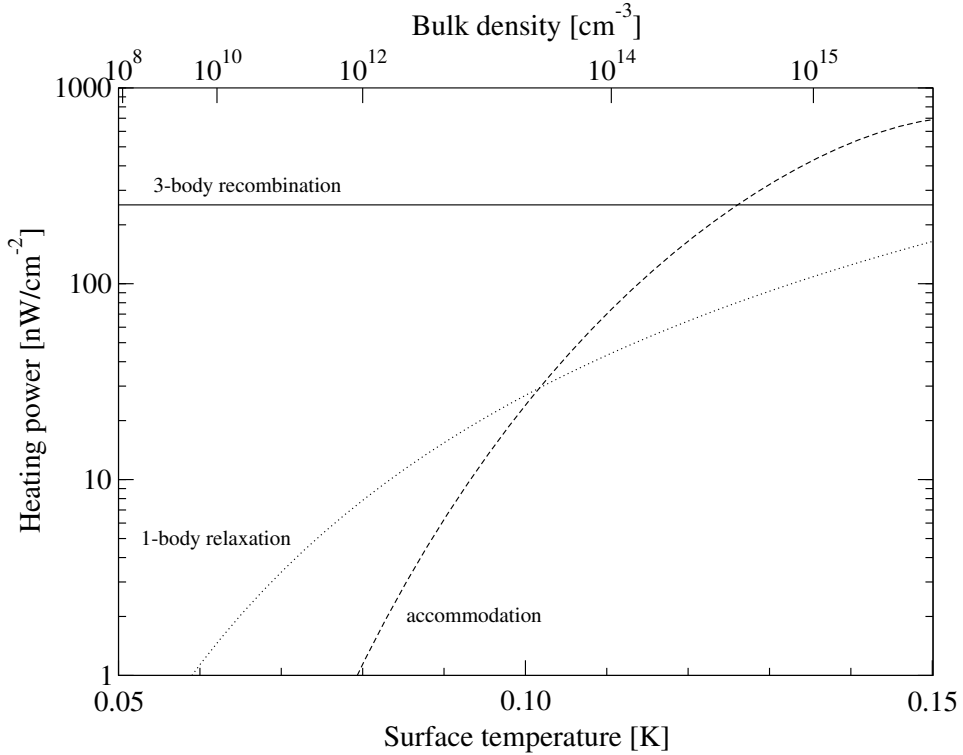
Figure 2: Calculated heating of a small surface spot from different sources as a function of the spot temperature: direct three-body recombination heating, one-body relaxation on the sample cell walls, and thermal accommodation of the bulk gas. The surface density is 3×10^{12} cm^{-2} and the bulk density is calculated from eq. (3) at $T_b = 170$ mK. The lowest experimental value $G^e = 8 \times 10^{-5}$ s^{-1} of this work was used to calculate the relaxation heating.

to the 2D case, is not so clear, and theories predict different reductions of L_3^s [15, 60]. A somewhat larger (but yet within the error bar) than a 3! fold decrease of L_3^s was observed in the magnetic compression experiments at Turku [20] and there seems to be a possibility to distinguish the effect from dimensionality on the three-body recombination rate.

1.2.4 Electron-spin resonance on H gas

For atomic hydrogen two transversely excited ESR transitions are allowed: $a \Rightarrow d$ and $b \Rightarrow c$ as presented in fig. 1. Their frequencies in high magnetic fields $B \gg 50$ mT are $\omega_R \approx (\pm 1/2 a_h + g_e \mu_b B)/\hbar = 2\pi(\pm 0.71 + 28 \times B/\text{T})$ s^{-1}. For a linearly polarized excitation field $B_1 \cos \omega t$ the time-dependent perturbation theory gives an ESR transition rate [68]

$$P_E = \frac{\pi}{8} \gamma_e B_1^2 \delta(B - B_0), \tag{9}$$

where γ_e is the electron gyromagnetic ratio and $B_0 \approx \omega_R/\gamma_e$ is the field at resonance. In practice, due to relaxation processes in the spin system, the delta function in eq. (9) needs to be replaced by an intrinsic line shape function f_i. The intrinsic relaxation processes of bulk H↓ are very slow, and the observed line shape is determined by inhomogeneities of the local magnetic field [69, 70, 71]. Yurke *et al.* [72] found, when considering different line broadening mechanisms, that the largest contribution to the bulk H↓ line shape is due to radiation damping [70, 73] yielding a constant line amplitude and a linewidth proportional to the density. In our experiments this effect is negligibly small for $n \lesssim 10^{15}$ cm^{-3}.

The power absorbed in unit volume from time dependent magnetic field in a lossy paramagnetic sample is expressed with the help of the complex susceptibility $\chi(\omega) = \chi'(\omega) - i\chi''(\omega)$ as [74]

$$P = \frac{\omega}{2\mu_0}\chi'' B_1^2, \tag{10}$$

where μ_0 is the vacuum permeability. Comparing equations (9) and (10) it is noticed that $\chi'' \propto nf_i$, and the density of paramagnetic particles can be extracted as

$$n = \frac{4}{\pi\mu_0\hbar\gamma_e^2} \int_0^\infty \chi''(\omega)d\omega. \tag{11}$$

In these ESR experiments the signal is detected at a fixed frequency ω_0 where the resonator is tuned. By sweeping ω or B the ESR line is measured. The relation between χ and the observed ESR signal S in an open Fabry-Perot resonator is derived below. Optical Fabry-Perot resonators are more conveniently described by the so-called coupled mode approach, found e.g. in ref. [75], than the equivalent RLC-circuit approach [74] used for closed resonators. However, following the coupled mode approach eventually gives the same result as derived for the RLC-circuit.

In the coupled mode approach the so-called mode amplitude $u(t)$ is defined. It is a complex variable normalized in such a way that $uu^* \equiv |u|^2$ equals the energy in the resonator. The resonance frequency of the mode is ω_0. The resonator is coupled to an incident wave $s_i \exp(i\omega t)$ which is normalized in such a way that $|s_i|^2$ is the power carried by the incident wave. The energy in the resonator dissipates causing a decay of the mode amplitude. There are two different types of power dissipation. The rate of intrinsic dissipation τ_0^{-1} is related to the power absorbed inside the resonator, and the rate of external dissipation τ_e^{-1} is due to a hole coupling the incident wave to the resonator. The quality factor of the loaded resonator can be expressed with the decay rates as $Q_l = \frac{1}{2}\omega_0(\tau_0^{-1}+\tau_e^{-1})^{-1}$.

The time dependence of u coupled to the incident driving field, provided the power losses are small, is given by the equation [75]

$$\dot{u} = i\omega_0 u - (\frac{1}{\tau_0} + \frac{1}{\tau_e})u + \sqrt{\frac{2}{\tau_e}}s_i e^{i\omega t}, \tag{12}$$

In a steady state the solution of eq. (12) is

$$u = \frac{\sqrt{\frac{2}{\tau_e}}s_i e^{i\omega t}}{\tau_0^{-1} + \tau_e^{-1} + i(\omega - \omega_0)}. \tag{13}$$

In ESR experiments a reflected wave s_r from the cavity is measured. The relation between s_i and s_r is expressed by the reflection coefficient of the resonator [75]

$$\mathcal{G}_0 \equiv \frac{s_r}{s_i} = \frac{\tau_e^{-1} - \tau_0^{-1} - i(\omega - \omega_0)}{\tau_e^{-1} + \tau_0^{-1} + i(\omega - \omega_0)}. \tag{14}$$

When a lossy magnetic sample is placed into the resonator it changes the resonance frequency and absorbs an amount $\omega\chi''(\omega)|u|^2$ of power. This changes the mode decay rate and the resonance frequency according to

$$\tau_0^{-1} + \tau_e^{-1} \rightarrow \tau_0^{-1} + \tau_e^{-1} + \frac{1}{2}\omega\eta\chi''(\omega)$$
$$\omega_0 \rightarrow \omega_0/\sqrt{1 + \eta\chi'(\omega)}. \tag{15}$$

The filling factor η is defined in the usual way as the ratio between the magnetic field square integrated over the sample volume and over the whole resonator [74]. When the changes in eq. (15) are included in eq. (14) the reflection coefficient at the center of the cavity resonance is given by

$$\mathcal{G} = \frac{\mathcal{G}_0 - i\eta Q_l \chi(\omega)}{1 + i\eta Q_l \chi(\omega)}, \tag{16}$$

where, assuming small $\eta\chi'$, an approximation $(1 + \eta\chi'(\omega))^{-1/2} \approx 1 - \eta\chi'/2$ has been used. The observed ESR signal S is proportional to the changes in the reflected voltage $(\mathcal{G} - \mathcal{G}_0)s_i$ from the resonator. The relative change δ of the voltage reflection coefficient is given by

$$\delta \equiv \frac{\mathcal{G} - \mathcal{G}_0}{\mathcal{G}_0} = \frac{2\tau_0}{\tau_e - \tau_0} \cdot \frac{i\eta Q_l \chi(\omega)}{1 + i\eta Q_l \chi(\omega)}. \tag{17}$$

This result is identical to the result obtained for a closed cavity e.g. in ref. [69]. The real (imaginary) parts of δ are proportional to the absorption and (dispersion) parts of S. From eq. (11) it is found for small n that

$$n \approx \frac{\tau_e - \tau_0}{\tau_0} \frac{2}{\pi\mu_0\hbar\gamma_e\eta Q_l} \int Re[\delta]dB. \tag{18}$$

For higher n the relation between χ'' and $Re[\delta]$ is not linear anymore, and n has to be

extracted from the dispersion signal [76] or by using the Kramers-Kronig relations [69].

2 Experiments on 2D H ↓

2.1 Experimental apparatus

2.1.1 Cryogenic setup

The experiments were carried out in a top-loading cryostat with two home-made refrigerators, a dilution refrigerator (DR) and a ^{3}He refrigerator. The former cools the sample cell (SC) and the latter a low-temperature dissociator as illustrated in fig. 3. The dissociator is a H atom source similar to that used by the Amsterdam group [77]. It is a helical resonator operating at 348 MHz at about 700 mK where the ^{3}He refrigerator has a larger cooling power than the still of the DR. The base temperature of the DR is 30 mK and its cooling power at 100 mK is 150 μW. The sample cell (SC) is located in the center of a superconductive magnet operating at 4.6 T.

The sample cell is thermally linked to the mixing chamber (MC) of the DR, but the link is weak enough to make it possible to measure the recombination power accurately. Due to the relatively long distance of about 40 cm from the MC to the SC mechanical thermal anchoring is not convenient for cooling a small cold spot in the cell. Therefore we employed the dilute ^{3}He $-^4$He stream of the DR from the mixing chamber as a "coolant" of the cold spot (CS). At a typical circulation rate of 100 μmoles/s the mixture has a relatively large specific heat and it flows at the speed of 2 cm/s in a 1.5 mm diameter tube. It allows us to change the CS temperature in a few seconds by heating the incoming coolant. The ESR resonator in the SC is connected to the cryogenic mm-wave component block of the ESR spectrometer [P4] with standard D-band waveguide. A piece of CuNi waveguide is installed to ensure thermal insulation. The block is thermally anchored to the 1K pot of the DR. A thermal accommodator of the H flux from the dissociator and the buffer volume for H↓ gas are cooled by a step heat exchanger of the DR.

Temperatures of the mixing chamber, the sample cell (T_{sc}), the buffer volume and the cold spot coolant (T_{liq}) are measured with RuO$_2$ chip resistors calibrated against the ^{3}He melting curve thermometer and NBS SRM 768 superconducting fixed-point device. The calibrations are estimated to be accurate to within 1 mK. Temperatures are monitored and adjusted with a.c. resistance bridges and temperature controllers (RV-Elektroniikka Oy) and computer-controlled lock-in amplifiers (Stanford Research Systems).

If the whole dilute stream of the DR would be used to cool the cold spot, the operation of the DR would be seriously disturbed at high T_{liq}. Therefore, the stream is divided into two approximately equal parts as illustrated in fig. 4. One of the streams is taken in a 1.5 mm
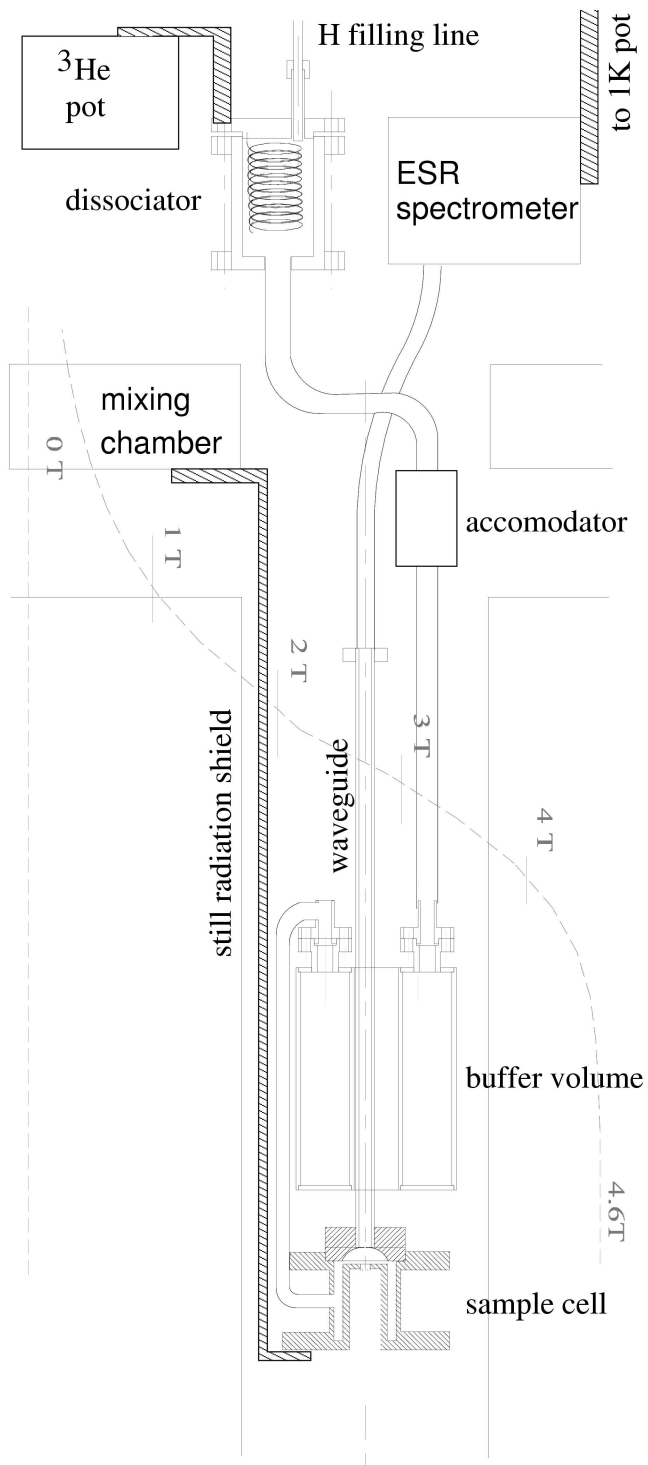
Figure 3: Scheme of cryogenic parts of the setup including sample cell (version SCI), buffer volume and dissociator. The dashed line indicates the value of the main magnetic field.
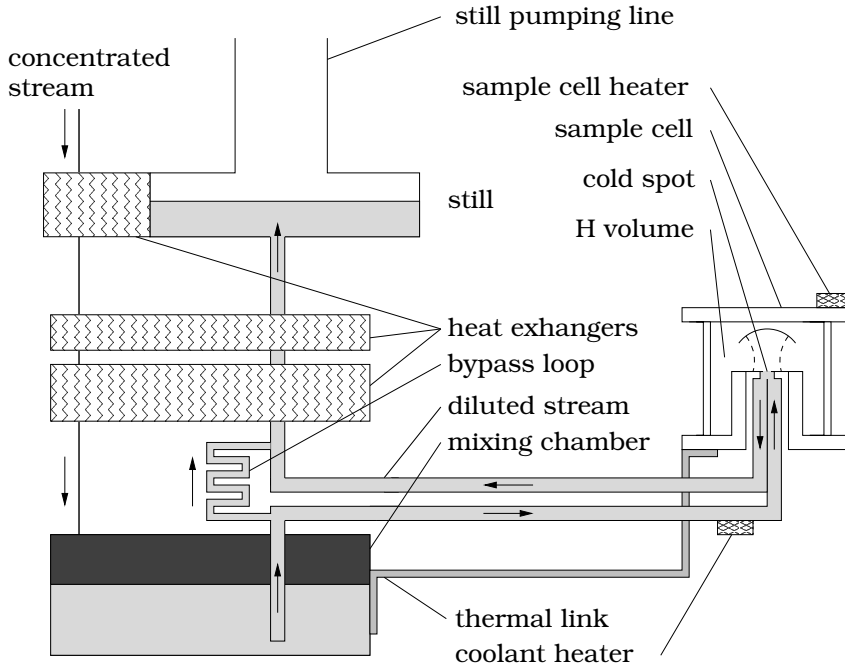
Figure 4: Cooling of the cold spot and the sample cell. The cold spot temperature is set by the cooling liquid temperature. A stable operation of the refrigerator is maintained by the by-pass loop in the dilute stream.

diameter stainless steel tube to the cold spot as described above. The other flows through a by-pass loop. Before entering the DR heat exchanger the two streams merge. In this way we can raise T_{liq} up to 300 mK while still being able to keep the SC and MC temperatures below 50 mK.

The calibration of the H↓ bulk density n is made calorimetrically by measuring the recombination heat liberated in the sample cell. A decrease/increase in the recombination power is compensated by the SC temperature controller, which keeps T_{sc} constant by increasing/decreasing the heating power P to the sample cell. In fig. 5 P is shown for several decays at different T_{liq}. The time variation of the bulk density is given by the relation

$$n(t) = \frac{2}{V_h D} \int_t^\infty [P_0 - P(t')]dt', \qquad (19)$$

where V_h is the volume of the sample cell, $D = 4.478$ eV is the dissociation energy of a single hydrogen molecule [35] and $P_0 \equiv P(\infty)$ is the stabilization power without H↓. The inaccuracy and the slow drift of P_0 are the main sources of error of the density calibration. For $n = 10^{14}$ cm^{-3} the error is about 10 %.
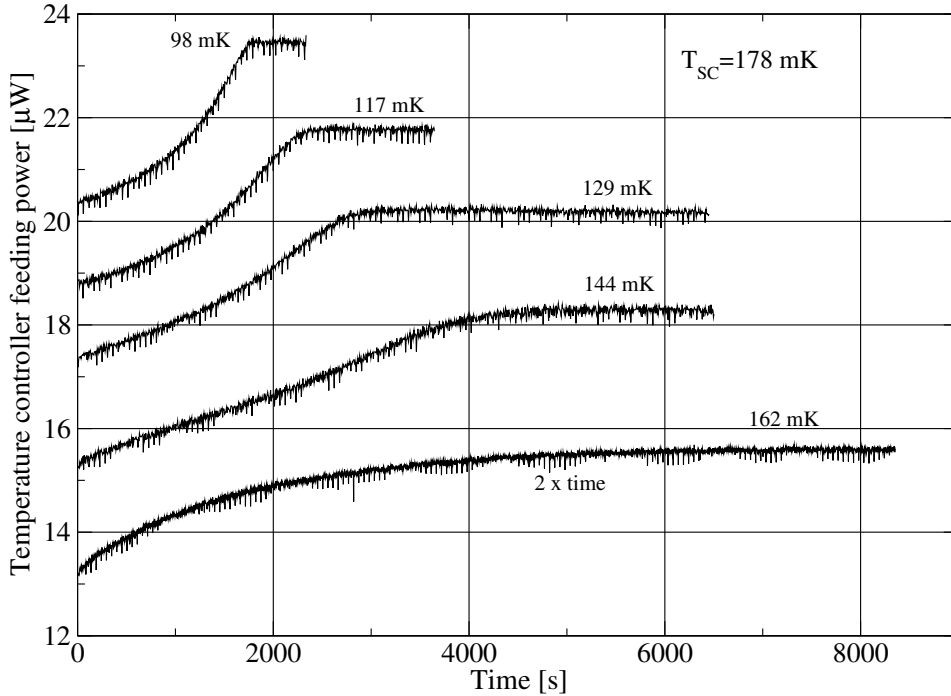
Figure 5: Signals recorded by the temperature controller on the total heating power $P(t)$ with SCII at $T_{sc} = 178$ mK for different cold spot coolant temperatures T_{liq} ranging from 98 mK to 162 mK. For the lowermost trace the time scale is multiplied by 2.

2.1.2 Sample cells and ESR spectrometer

Two versions of the sample cell, hereinafter called SCI and SCII, were used in this work. The main difference between SCI and SCII is the size and position of the cold spot in the ESR resonator. Schematic drawings of the cells are shown in fig. 6. In both variants the resonator is of the open geometry Fabry-Perot type, which is similar to the optical resonator used in lasers [78]. The open geometry was chosen to ensure a free escape of recombination products from the CS. The upper mirror of the resonator is hemispherical with 6.5 mm radius of curvature, while the lower mirror is planar. The coupling of mm-wave energy between the SC and a standard rectangular D-band waveguide is through a 0.5 mm diam. orifice in the center of the spherical mirror. Both cells were made of high-purity Cu and carefully etched in order to reduce impurity-induced $b - a$ relaxation. The other materials used were high-purity gold, indium, Kapton and Mylar polymer films, teflon tubes and Stycast 1266 epoxy.

When designing the sample cell for thermal compression experiments we were aware of the high three-body recombination rate on the CS leading to a fast density decay and consequent strong recombination heating of the sample. Estimates of these effects were
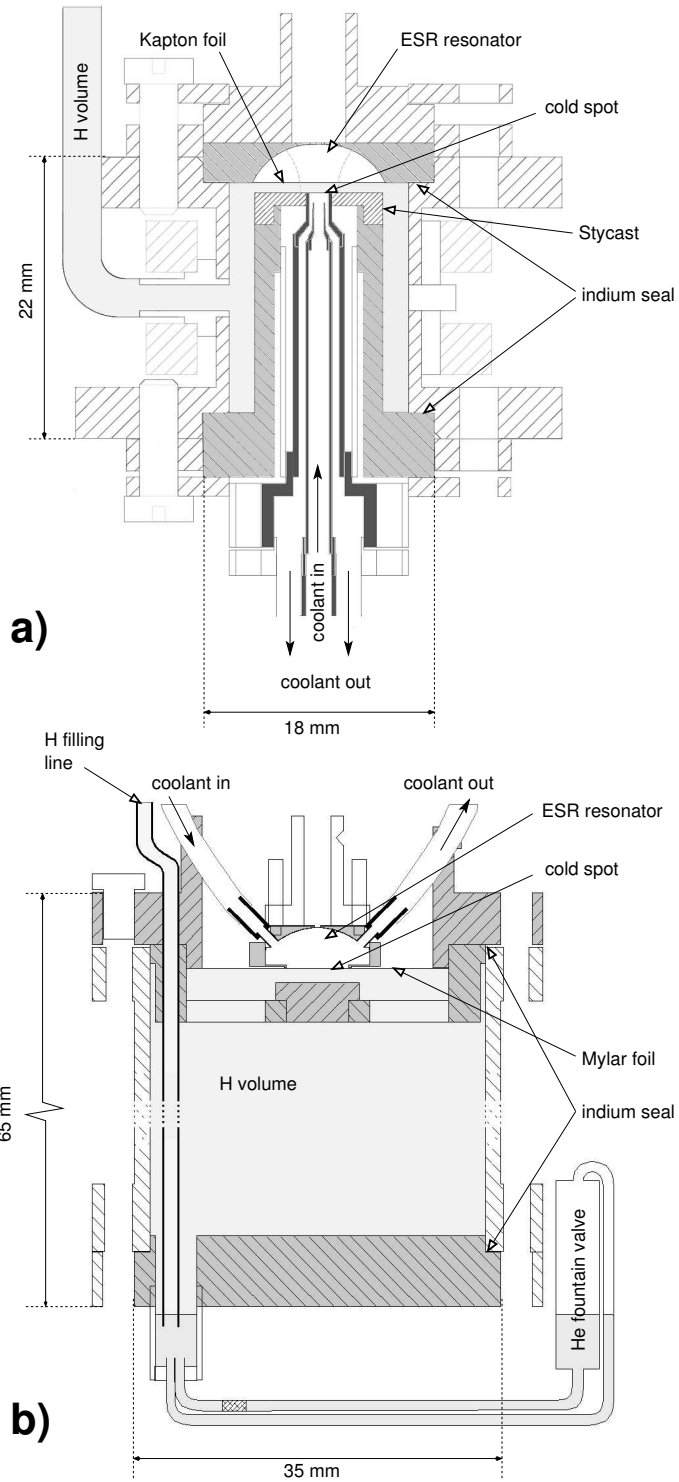
Figure 6: Two sample cell variants. a) SCI with 1.5 mm diameter cold spot located in the middle of the flat mirror of the resonator. b) In SCII with 6 mm diameter cold spot located on the lower surface of Mylar film forming the upper surface of the SC.

based on the experimental value $L_3^s = 2 \times 10^{-24}$ cm^{4}s^{-1} [51, 52, 79] of the three-body loss rate constant, as known at the time of the design of SCI. Together with the buffer volume of 38.5 cm^3 this fixed the optimal choice of the CS diameter to 1.5 mm, so that the lifetime of the sample would still be of the order 10^3 s.

In SCI the cold spot is located in the center of the flat mirror of the resonator where also the maximum of the ESR excitation field B_1^2 lies. The resonator operates in the TEM$_{002}$ mode with $Q_l \approx 2700$. The 3.2 mm diameter of the ESR excitation field is larger than the CS size, which allows the detection of surface atoms outside the CS. The flat mirror of the ESR resonator is made of a 1 μm thick gold layer evaporated on a 13 μm thick Kapton foil. The latter is glued on a 0.6 mm thick epoxy disk which has a 1.5 mm diameter hole in the center. In the hole there are two concentric thin-walled copper tubes in which the ^{3}He-^{4}He mixture stream flows to and from the lower surface of the foil to cool the CS region. To avoid distortions of the ESR line shape due to too large a number of H atoms [76] the volume of the bulk gas is restricted by another Kapton foil placed 0.8 mm above the flat mirror. Hydrogen atoms are fed from the buffer volume to the SC through a 5 cm long Teflon tube. The buffer volume temperature is kept at about 350 mK, which is ideal for storing H↓ atoms.

A series of experiments carried out [P1, P2] led to a better understanding of the behaviour of 2D H gas and revealed certain disadvantages in the construction of SCI. The most important result was that the three-body recombination rate on the CS turned out to be much smaller than expected. Three-body recombination was not dominating the decay and in fact the contribution of the CS was hardly discernible from the one-body relaxation rate on the sample cell and buffer volume walls. By "switching" the thermal compression on and off during the decays we extracted an upper limit estimate $L_3^s \lesssim 2 \times 10^{-25}$ cm^{4}s^{-1} [P2], which is 10 times smaller than expected. Also the thermal contact between the spot and the cell in SCI was too strong, not allowing to work with a large enough temperature difference between the CS and the SC. Lowering T_{sc} strongly increased the one-body relaxation rate. Another drawback was that the ESR line shape of 2D hydrogen on the CS was distorted by the inhomogeneous density distribution, which depends on the temperature difference between the spot and the cell.

In the later version of the sample cell, SCII (fig. 6b), the CS radius is increased to 3 mm. The "ceiling" of the H volume is a 20 μm Mylar film. An epoxy ring together with the spherical mirror is glued on the top of the center of the Mylar foil, outside the H volume, forming a space filled with circulating ^{3}He-^{4}He mixture. This construction improves the thermal insulation between the CS and the SC. The horizontal extent of the ESR excitation field on the CS is smaller than the cold spot which makes the ESR signal originate from the central part of the CS only. This decreases the line broadening due to a possible density

inhomogeneity and gives an opportunity to study the intrinsic line shape. Due to good thermal isolation between the CS and the SC we are able to work at higher cell temperatures. This made it also possible to remove the buffer volume and to increase the volume of the cell to 40 cm^3. The cell geometry is designed to be simple, making it easier to cover its inner surfaces with a polymer foil and epoxy. These measures allowed us to reduce the one-body relaxation rate to a negligible level. To avoid the escape of atoms and excited molecules from the SC, we installed a ^{4}He fountain valve into the H filling line. The valve is controlled with a heater and the helium level is measured with a capacitive level gauge.

The ESR resonators were designed to detect both 3D gas in the cell volume and 2D gas adsorbed on the CS. They were constructed relying upon the Gaussian beam wave theory for laser resonators [78]. When a proper resonance mode was found, the excitation field profiles $B_1^2(\mathbf{r})$ were calculated numerically by solving the Helmholtz equation with ideally conducting boundary conditions. The calculation of $B_1^2(\mathbf{r})$ in SCI was compared with measurements of $B_1^2(\mathbf{r})$ carried out with an oversized test resonator [P5]. $B_1^2(\mathbf{r})$ was used when calculating the effective volume of the resonator from the relation

$$V_e = \frac{1}{\max[B_1^2]} \int B_1^2(\mathbf{r}) d^3 r, \tag{20}$$

where the integral is taken over the hydrogen volume in the resonator. The effective area A_e of the CS is calculated similarly by integrating over the area of the flat mirror. The values of V_e and A_e are important in the calibration of the ESR signals against the bulk and surface densities.

The resonator of SCII is shown in fig. 7 together with the calculated $B_1^2(\mathbf{r})$. The resonator operates in the TEM$_{003}$ mode and its Q_l is about half of that of SCI. The field profile in the resonator is distorted by the dielectric Stycast part and it is not very well described by the Gaussian beam wave theory. These disturbances can be seen in the two lowest nodes in fig. 7. Three quarters of the resonator is filled with the coolant liquid whose dielectric constant 1.05 depends slightly on the ^{3}He/^{4}He concentration ratio which together with the resonator frequency depends on temperature. Fortunately this dependence is rather weak at $T_{liq} \lesssim 100$ mK and does not noticeably disturb the stability of the ESR signal. On the other hand, by heating the coolant to temperatures of the order of 1K leads to an ESR resonator frequency shift of about 50 MHz and helps to find the resonance frequency after the cool down of the spectrometer from room temperature. The ESR spectrometer is a home-built 129 GHz cryogenic heterodyne system. Its technical details are described in ref. [P4]. The spectrometer is capable of detecting simultaneously both absorption and dispersion signals with the detection sensitivity of about 10^9 spins/G for 20 pW mm-wave excitation power.
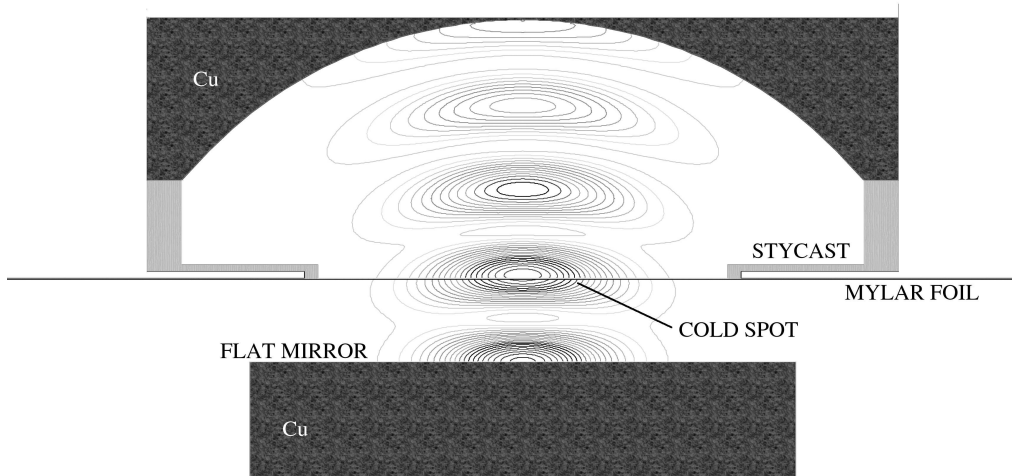
Figure 7: Resonator in SCII and contour plot of the calculated excitation field intensity $B_1^2(\mathbf{r})$. The contours are drawn for every 1/20 intensity change. The volume for the hydrogen gas in the resonator is limited between the flat mirror and the CS. The space between the spherical mirror and the Mylar foil is filled with ^{3}He-^{4}He coolant mixture.

2.2 Measurement procedures

2.2.1 Production and decay of atomic hydrogen

Pulsed RF discharge is used to dissociate H_2 molecules into H atoms in a discharge cell called dissociator. Before the actual experiment the dissociator is loaded from room temperature with H_2 gas through a thermally insulated capillary to form a layer of solid H_2 on the walls of the dissociator. During the measurements the walls of the dissociator and the SC are lined also with a superfluid helium film. Applying 1 ms long 0.1 W RF pulses to the dissociator at a repetition rate of 100 Hz yields a H↓ flux of about 2×10^{13} atoms/s to the sample cell. It takes usually about 2000 s to reach the saturation bulk density of about 10^{15} cm^{-3}. During the accumulation of the H↓ sample the MC and the SC are overheated due to helium vapour recondensing and hydrogen recombining in the filling line. After switching off the dissociator a-state atoms disappears in a few minutes and the H↓↕ sample is ready. At the same time the mixing chamber, sample cell, and CS coolant temperatures are stabilized to their desired values.

Most experiments in this work were measurements of the density decay. The experimental conditions could be changed from one decay to another, including T_{sc} and T_{liq}, thicknesses of the ^{4}He film and of the solid H_2 layer on the cell walls as well as the ESR excitation power. Due to the large surface area of the cell the bulk gas temperature $T_b \approx T_{sc}$. The feedback power of the temperature controllers and the ESR spectra were registered
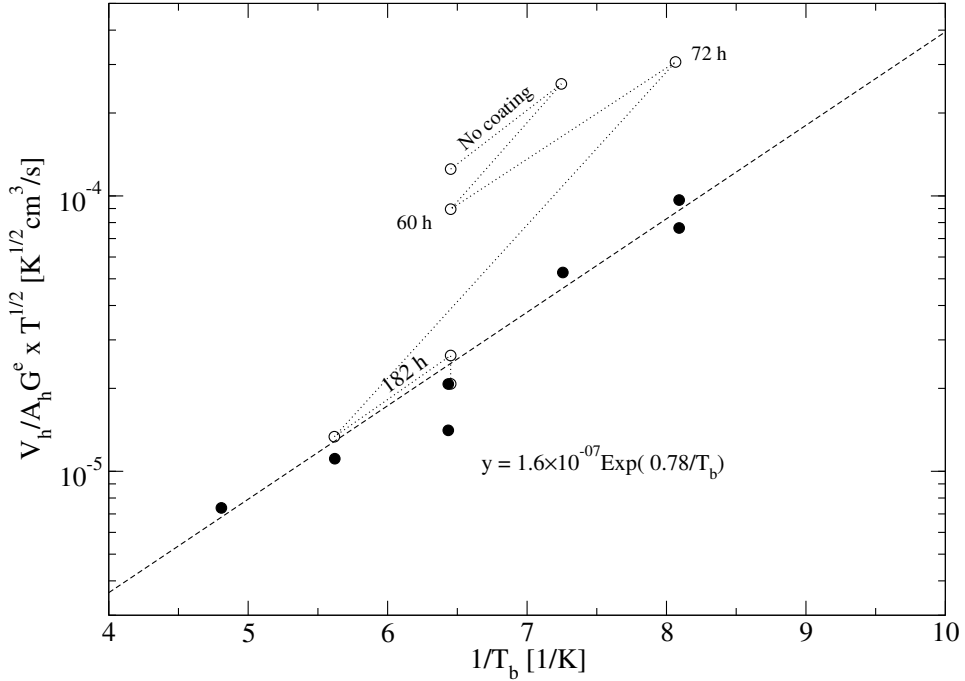
Figure 8: $\frac{V_h}{A_h}G^e\sqrt{T_b}$ plotted versus $1/T_b$ with different accumulation times for the solid H_2 layer. The closed circles are the saturated values after accumulating for 300 hours or more. The dashed line is an exponential fit to the saturated values. The open circles show results for shorter accumulation times as indicated. The dotted lines display the temporal sequence in which the open circles were measured.

during the decay. In order to determine the power P_0 needed in the density calibration (eq. (19)) the data collection was continued until the atomic hydrogen signal had become completely extinct. The spectra were obtained by sweeping the magnetic field across the bulk and surface $b - c$ resonances.

The ESR excitation power could be varied within four orders of magnitude. The ESR-induced recombination of the sample was used to estimate the absolute value of the field B_1 (eq.(9)) in the resonator. At the highest excitation levels we observed $B_1 \approx 10^{-2}$ G. When the excitation was lowered by an order of magnitude, the destruction of the sample due to ESR was negligible compared to the natural decay rate. However, another order of magnitude decrease was required to avoid the instability effects in the 2D ESR signals [P1].

The rate of $b - a$ nuclear relaxation is influenced by the quality of the sample cell walls. Although much care was taken to reduce the amount of possible magnetic impurities in the walls, the relaxation rate was always high in the beginning of each series of experiments. Therefore we used the well-known method [80] to build up a layer of solid H_2 on the SC walls by keeping the H↓ flux continuously on even for a week. This decreased the relaxation
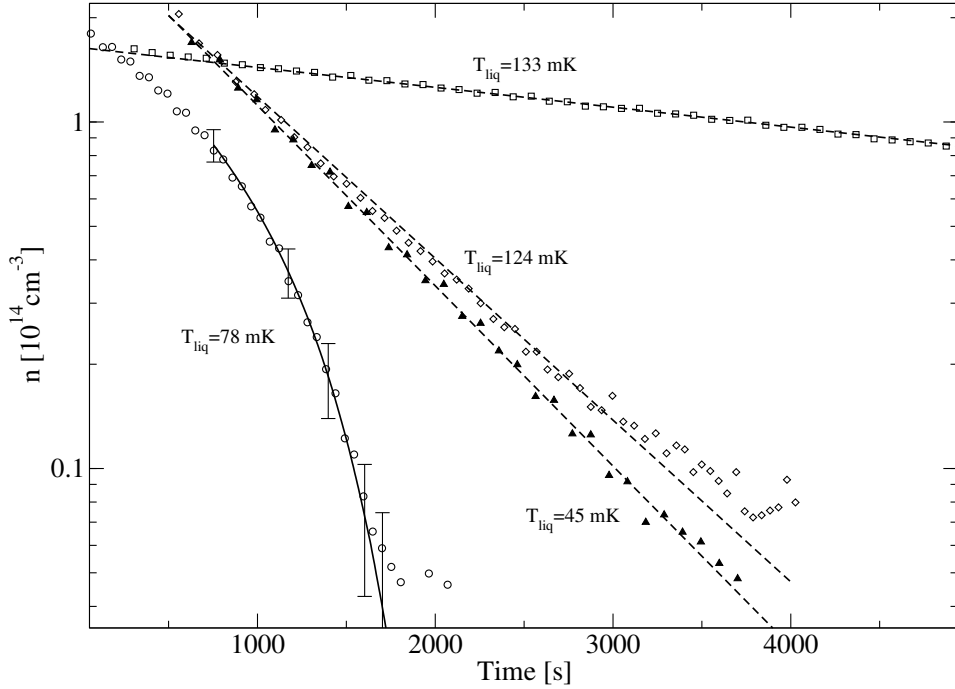
Figure 9: Decay of *b*-state density extracted from ESR spectra. In SCI at $T_{sc} = 124$ mK, ▲-$T_{liq} = 45$ mK, ◇-$T_{liq} = 124$ mK. In SCII at $T_{sc} = 178$ mK, ∘-$T_{liq} = 78$ mK, □-$T_{liq} = 133$ mK. The solid line with error bars is from a calorimetric density calibration, the dashed lines are exponential fits to ESR data points. The decay at $T_{liq} = 78$ mK in SCII is not exponential because of the high three-body recombination rate on the CS.

rate by an order of magnitude. The intrinsic one-body relaxation rate ultimately obtained in both sample cells was lowest ever reported for atomic hydrogen experiments [51, 81]. The change of the relaxation rate in SCII after different H_2 coating times is presented in fig. 8. The density of a H_2 monolayer is about 10^{15} cm^{-2} which gives an estimate of 0.15 nm/h for the growth of the H_2 layer. The relaxation rate appears to saturate at the value $G^e = 1.6 \times 10^{-7} \times \frac{A_h}{V_h} \sqrt{T_b}^{-1} \exp(0.78/T_b)$ after 200 hours of coating when the H_2 layer is about 30 nm thick.

Examples of raw data obtained in decays of H↓↕ after saturation H_2 coating are shown in fig. 9. An influence of T_{liq} on the total decay rate of the sample in SCI and SCII is well demonstrated. The difference between the "warm" and "cold" spot decays is very small for SCI, which is due to the unexpectedly slow three-body recombination and the small area of the CS. In SCII most of the atoms are recombining on the CS, the area of which is only 0.3% of the total surface. For the absolute calibration of the ESR signal we need to find the proportionality coefficient (C_1 in eq. (21)) between the density and integrals of the ESR peaks. This is found by multiplying the whole set of ESR data points (peak integrals) by the

constant C_1 and fitting it to the integrated temperature controller signal with C_1 being a free parameter. Decays with the warm spot are very well described by exponential functions. This implies that the temperature of the cell walls remains constant during the decays and that the decays are of the first order in density as caused by one-body relaxation.

2.2.2 ESR spectrum of bulk and surface hydrogen gas

In this work ESR spectra of H↓↕ were recorded by repetitively sweeping the magnetic field through the surface and bulk $b \rightarrow c$ resonances. The sample decays in a time of $10^3 - 10^4$ s which allows to collect 50-100 spectra using sweep times from 50 to 200 s. When the CS is warm, only one peak originating from the bulk gas is visible in the spectrum. A peak from the surface adsorbed atoms, shifted to higher sweep field values, appears after activation of the thermal compression. This is seen in the first spectrum of fig. 10 as a smaller surface peak shift, when the CS is still cooling to a proper temperature. The separation of the peaks is proportional to the density according to eq. (2). The densities of the bulk and surface sample decay with time and the surface peak moves towards the bulk one.

Both the absorption and dispersion components of the ESR signal were recorded. For a linear system they are related through the well-known Kramers-Kronig relations. The cease of the Kramers-Kronig relations between the signal components revealed all nonlinear distortions of the signal. At the densities $\leq 10^{15}$ cm^{-3} the bulk line shape remains unchanged and its amplitude is proportional to the density of the bulk atoms n. The shape of the bulk line is determined by the inhomogeneity of the main magnetic field. Using two shim coils mounted on the still radiation shield of the DR we were able to reduce the axial inhomogeneity to about 0.1 G/mm.

The equation obtained from eq. (10) describing the bulk absorption line shape is given by

$$S_n(B) = C_1 \int n B_1^2(\mathbf{r}) f(B(\mathbf{r}) - B_0) d^3 r, \tag{21}$$

where the constant C_1 is extracted from the calorimetric calibration eq. (19) and $B(\mathbf{r})$ is the polarizing field including possible inhomogeneities. The function f is the normalized line shape function which is a convolution of the intrinsic line shape f_i (discussed in 3.1.2) and the spectral line of the mm-wave source f_e

$$f(\omega_0) = \int f_i(\omega_0 - \omega) f_e(\omega) d\omega. \tag{22}$$

If the function f is narrow enough, it can be approximated by a delta function and then eq. (21) gives a possibility to image the mm-wave field $B_1^2(\mathbf{r})$ in the resonator by applying the known gradients of the polarizing field $B(\mathbf{r})$. In fig. 11 the response of the line to the
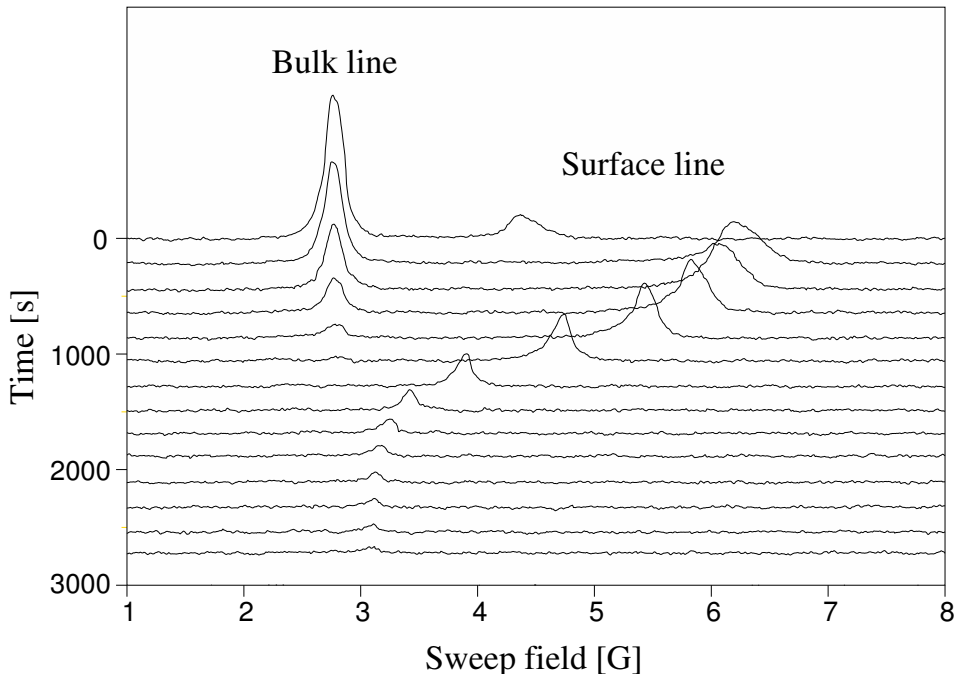
Figure 10: Evolution of $b \rightarrow c$ absorption spectra recorded at low excitation power with SCII at $T_{sc} = 178$ mK and $T_{liq} = 78$ mK. Every curve is a single sweep through the resonance completed in 50 s. The delay between the sweeps is 200 s. The starting time for each sweep is indicated on the vertical axis. The temperature is not yet stabilized during the first sweep which is the reason for the smaller surface density in this case.

applied magnetic field gradient is demonstrated. The bulk line is split into two peaks. The left one corresponds to the B_1^2 antinode near the CS and the right one to the antinode close to the flat mirror. The surface line is not influenced by the axial gradient. The bulk peaks were integrated separately and the values were compared to the integrals over the corresponding $B_1^2(\mathbf{r})$ field antinodes from the numerical calculations (fig. 7). The resonator length and the position of the Kapton foil were varied to get the best correspondence between the calculations and the measured values. In this way the values of A_e and V_e for SCII could be extracted more reliably.

The equation describing the surface line shape is similar to eq. (21), but the volume integral is changed to an integral over the CS area. We also have to take into account that the argument of f contains the dipolar field term $B_d(\mathbf{r}) = \alpha_d \sigma(\mathbf{r})$ from eq. (2). Then the equation for the surface line shape is

$$S_\sigma(B) = C_1 \int \sigma B_1^2(\mathbf{r}) f(B(\mathbf{r}) + B_d(\mathbf{r}) - B_0) d^2 r. \tag{23}$$

The surface resonance line can be broadened by an inhomogeneous density distribution

32
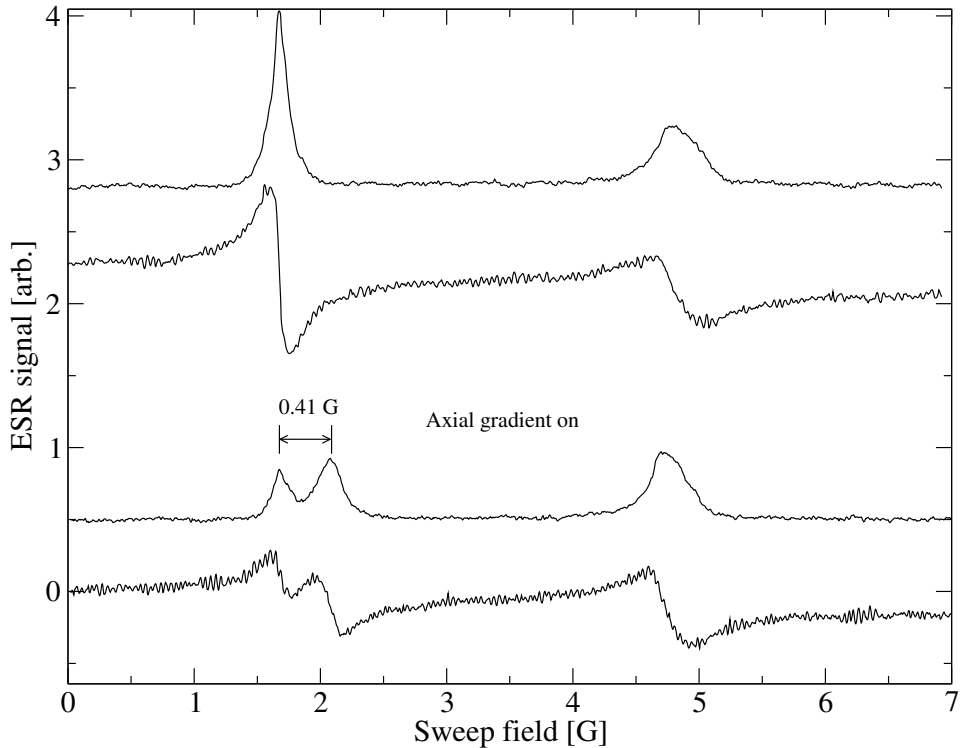
Figure 11: Absorption and dispersion spectra recorded with SCII at $T_{sc} = 138$ mK and $T_{liq} = 78$ mK. The density of bulk and surface atoms is $n = 6.3 \times 10^{13}$ cm^{-3} and $\sigma = 3.1 \times 10^{12}$ cm^{-2}, respectively. In the lower pair of spectra an axial magnetic field gradient of 0.37 G/mm is applied to split the bulk peak into two parts originating from two different $B_1^2(\mathbf{r})$ antinodes.

$\sigma(r)$. This was clearly observed in the experiments in SCI where the spatial extent of the $B_1^2(\mathbf{r})$ field antinode was larger than the CS diameter [P2].

3 Results

3.1 ESR line shape of adsorbed hydrogen

3.1.1 ESR instability

The first ESR experiments on 2D H↓ were performed at the University of British Columbia by Hardy and coworkers [30]. They observed that the ESR line of adsorbed atoms was asymmetric and much broader than the bulk line. As one of the possible explanations for the observed line shapes they suggested the so-called ESR instability found in ferromagnetic resonance experiments of solids in strong magnetic fields [82, 83]. However, a quantitative study of the line shapes was not possible due to fast recombination of the H↓ samples

33
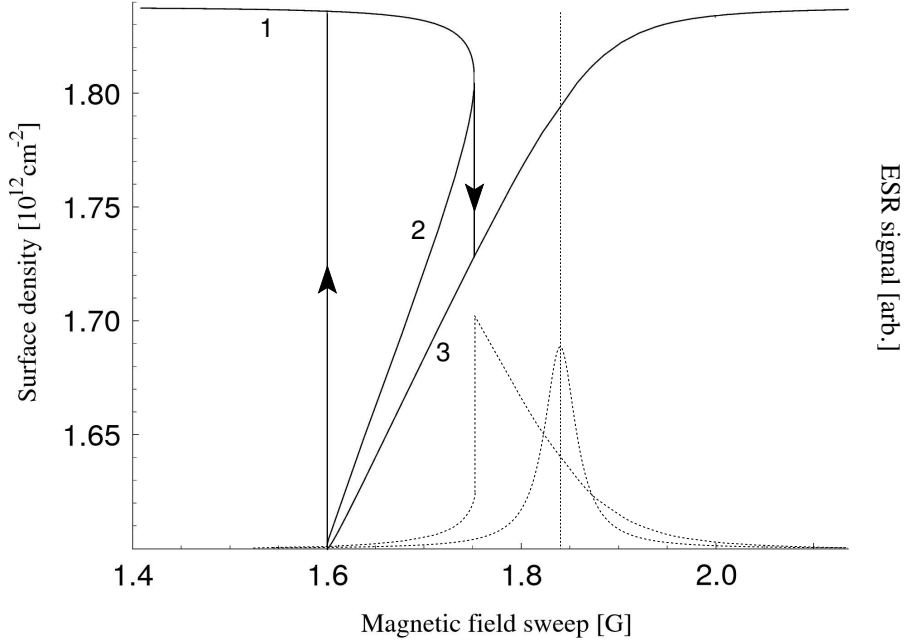
Figure 12: Surface density σ (solid line) and ESR signal (dashed line) calculated for a high excitation power as a function of the magnetic field sweep ΔB. The arrows show the jump-like response of the surface density and ESR signal for different directions of the sweep field. The parameters used in this calculation were: $T_\sigma = 90$ mK, $B_1 = 0.35$ mG, $\Gamma = 40$ mG and $n = 10^{13}$ cm^{-3}. The undisturbed resonance line position is 1.84 G. The numbers 1, 2, and 3 correspond to different roots of eq. (24) (see text).

and low sensitivity of detection. Similar 2D line shapes were observed also in this work for comparatively large ESR excitation powers [P1]. When the ESR excitation level was decreased the asymmetry disappeared, which indicated that the line shape was modified by the excitation field disturbing the magnetization of the 2D spin system.

The change of surface density can be written as the difference between the adsorbing and desorbing fluxes of atoms. The former flux is simply $(1/4)nvs$, where s is the sticking probability, and the desorbing flux is proportional to eq. (4). Including also the ESR-induced recombination time τ_{ESR} we get

$$\dot{\sigma} = \frac{1}{4}nvs - (\frac{1}{\tau_r} + \frac{1}{\tau_{ESR}})\sigma, \tag{24}$$

where $\tau_{ESR}^{-1} = 2\frac{\pi}{8}\gamma_e B_1^2 f(\Delta B - \alpha_d\sigma)$ follows from eq. (9) when the δ function is replaced by the normalized line shape function f and $\alpha_d\sigma$ is the intrinsic mean dipolar field given by eq. (2). The linewidth Γ of surface atoms is of the order of 50 mG which gives $\tau_{ESR} \approx \tau_r$ at 100 mK for $B_1 \approx 1.6$ mG corresponding to the excitation power of about 3 nW. Thus even

quite a small ESR excitation can disturb the dynamic equilibrium between bulk and surface atoms.

To get a better understanding of the connection between the line shape and the ESR excitation one should examine eq. (24) more closely. The undisturbed line shape function f of the surface atoms is assumed to be Lorentzian as supported by the measurements at low excitation power. In equilibrium $\dot{\sigma} = 0$ and σ has three different roots denoted by the numbers 1 to 3 in fig. 12 and $\sigma_0 \equiv \sigma(\Delta B)$ when $\tau_{ESR} = 0$. Because the analytic solutions are quite lengthy, it is more informative to present the qualitative behavior of $\sigma(\Delta B)$ instead. When the condition $\tau_{ESR} \approx \tau_r$ is valid, $\sigma(\Delta B) \leq \sigma_0$ and the resonant field $\alpha_d \sigma(\Delta B)$ is moved closer to the bulk line position at $\Delta B = 0$. If B_1 is still rather small, eq. (24) has only two roots, solutions 1 and 3 in fig. 12. The surface line is pulled towards the bulk line but there is no hysteresis. A further increase of B_1 results in stronger line pulling and in the appearance of the root 2 as a mark of the hysteresis of the spectrum. The response of $\sigma(\Delta B)$ is different for different sweep directions (cp. fig. 12).

For a more quantitative picture we extract $\sigma(\Delta B)$ just at the "tip" between the solutions 2 and 3 in fig. 12. Solving eq. (24) yields the relation

$$\sigma_t = \sigma_0 (1 + \frac{\gamma_e B_1^2 \tau_r}{2\Gamma})^{-1}, \tag{25}$$

where the intrinsic line shape of width Γ is assumed to be Lorentzian. The position of the ESR signal "jump" for a sweep towards the bulk line is $\sigma_t \alpha_d$. The amount of line pulling is determined by the combination of three quantities B_1^2, Γ and τ_r. The first one is rather clear, a strong excitation produces larger pulling. The effect of Γ means that for a narrower atomic resonance, ESR-induced recombination is larger, as can be seen from the definition of τ_{ESR}. The third quantity, τ_r, determines how long the atom resides on the surface. If τ_r is large then the ESR transition is more probable. Therefore in a colder gas the ESR instability sets in at a lower B_1. The critical excitation power for the instability to show up is

$$B_1^2 \gtrsim \frac{\Gamma^2}{\alpha_d \sigma_0 \gamma_e \tau_r}, \tag{26}$$

when the line pulling is about $\Gamma/2$. This condition defines the maximum ESR excitation field for detecting the natural line shape of surface atoms. The appearance of an instability can also be seen if both the absorption and dispersion parts of the ESR signal are detected. As mentioned above these signals are related through the Kramers-Kronig relation which is valid for a linear system. The correlation between the absorption and dispersion signal is lost when the instability takes place.
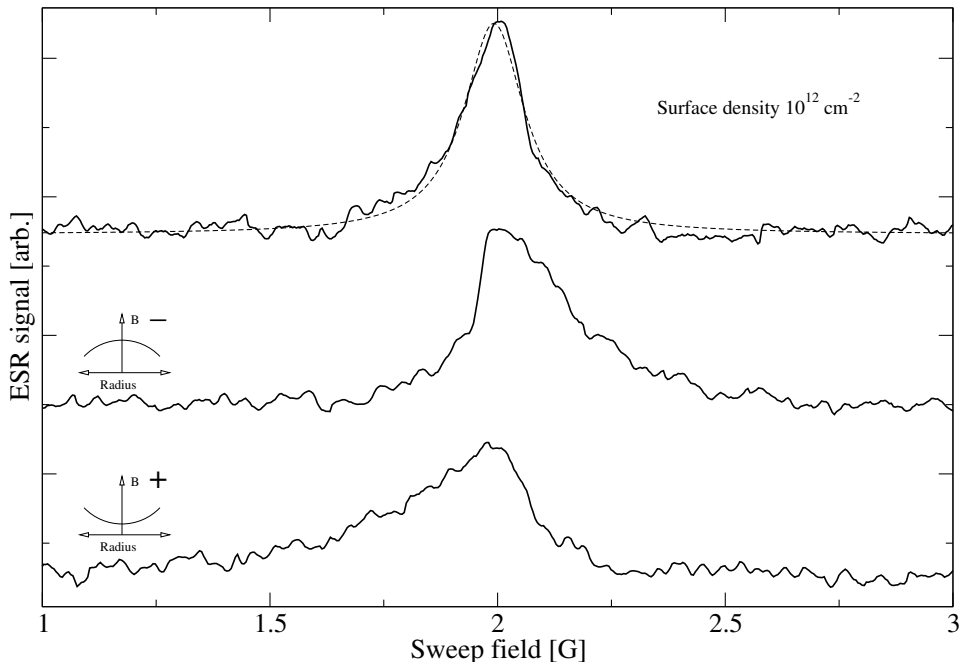
Figure 13: ESR line shapes of 2D H with $\sigma = 10^{12}$ cm^{-2} and $T_{liq} = 78$ mK measured in SCII. The two lower lines are distorted by the applied radial magnetic field gradients equal in amplitude but opposite in polarity. The uppermost line is measured without gradient and the dashed line is a fitted Lorentzian function.

3.1.2 Line broadening due to magnetic field inhomogeneities

Next we consider the inhomogeneity of the magnetic field and the frequency instability of the mm-wave source (MWS) as the origin for the ESR line broadening in the limit of small excitation power. The field inhomogeneity can originate from that of the external magnetic field and from the internal dipolar field which is inhomogeneous due to the uneven density distribution of H atoms adsorbed on the cold spot. These do not only contribute to the linewidth but also make the line asymmetric. The surface ESR line shape is described by eq. (23), where according to eq. (22) the line shape function f is a convolution of the intrinsic line shape and the frequency spectrum of the MWS. We found that the width of the MWS spectrum depended on the operating frequency: In some experimental runs its contribution to the linewidth was discernible but in most cases insignificantly small.

In comparison to the bulk line, the surface line is sensitive only to radial gradients of the magnetic field. The gradients are caused by field inhomogeneities of the main magnet and the ESR sweep coil and by the various magnetization of materials in the vicinity of the CS. An uneven density distribution also leads to an inhomogeneous intrinsic dipolar field $\alpha_d \sigma(r)$ over the cold spot. Changes in temperature, flow of atoms on the surface, and
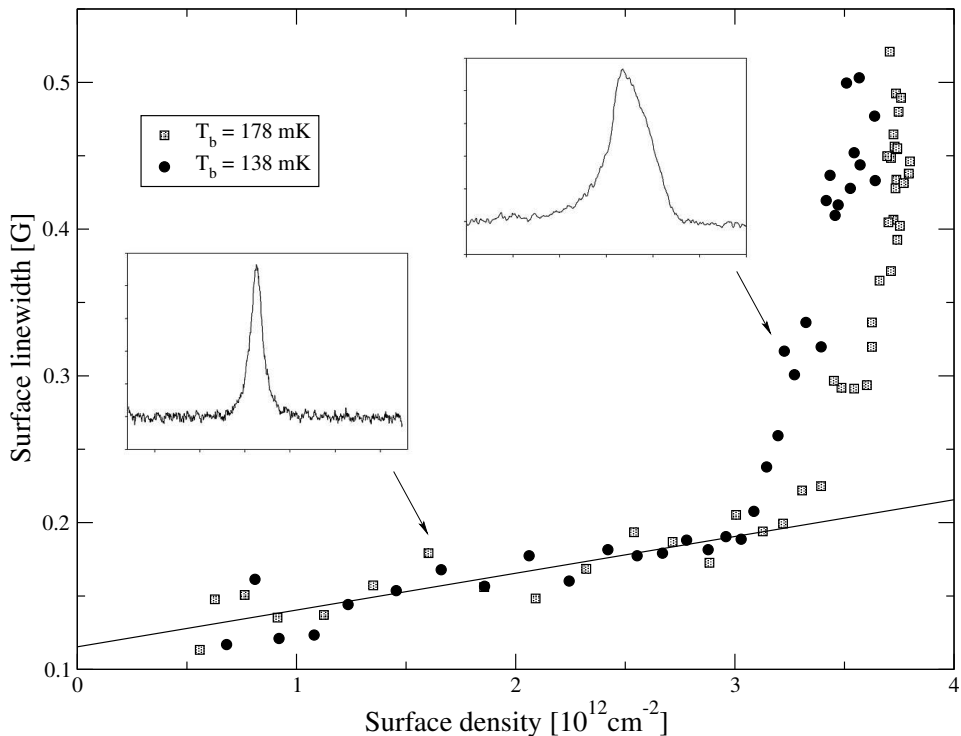
Figure 14: Surface linewidth (FWHH) measured at two different sample cell temperatures. A linear fit to the values below 3×10^{12} cm^{-2} (solid line) indicates a zero density linewidth of 115 mG and a broadening of $2.5 \times 10^{-14}\sigma$ Gcm^2. The zero density linewidth in this measurement is probably caused by the residual inhomogeneity of the main polarizing field, combined with the frequency spectrum of the mm-wave source. The insets shows two line shapes as examples demonstrating the appearance of the asymmetry (same horizontal scale).

surface roughness influence $\sigma(r)$ and lead to changes in the internal dipolar field and line shape during the decay of the H density [P2]. In SCI thermal isolation of the cold spot was inadequate, and instead of a step-like change of temperature near the edge of the CS there was a temperature profile which depended on the magnitude of $T_{liq} - T_\sigma$. The smallest surface linewidth was about 50 mG observed at $T_{liq} \approx T_\sigma$. On the other hand, due to the small size of the CS, we were able to extract $\sigma(r)$ from the observed line shapes [P2].

In SCII the sensitive ESR region was larger, which for a given field inhomogeneity gave a twice larger linewidth than for SCI. To compensate the radial field inhomogeneity a gradient coil was installed into SCII. The coil was wound around the CS and it was capable of producing a radial gradient $\frac{\partial B_z}{\partial r}$ of about 240 mG/(mm·A). Fig. 13 demonstrates the effect of the applied gradient on the surface line shape. The spectra were recorded for a low and relatively uniform adsorbed H density. Without the gradient we got a symmetric line shape close to a Lorentzian as shown in figs. 13 and 16. The gradient made the line asymmetric
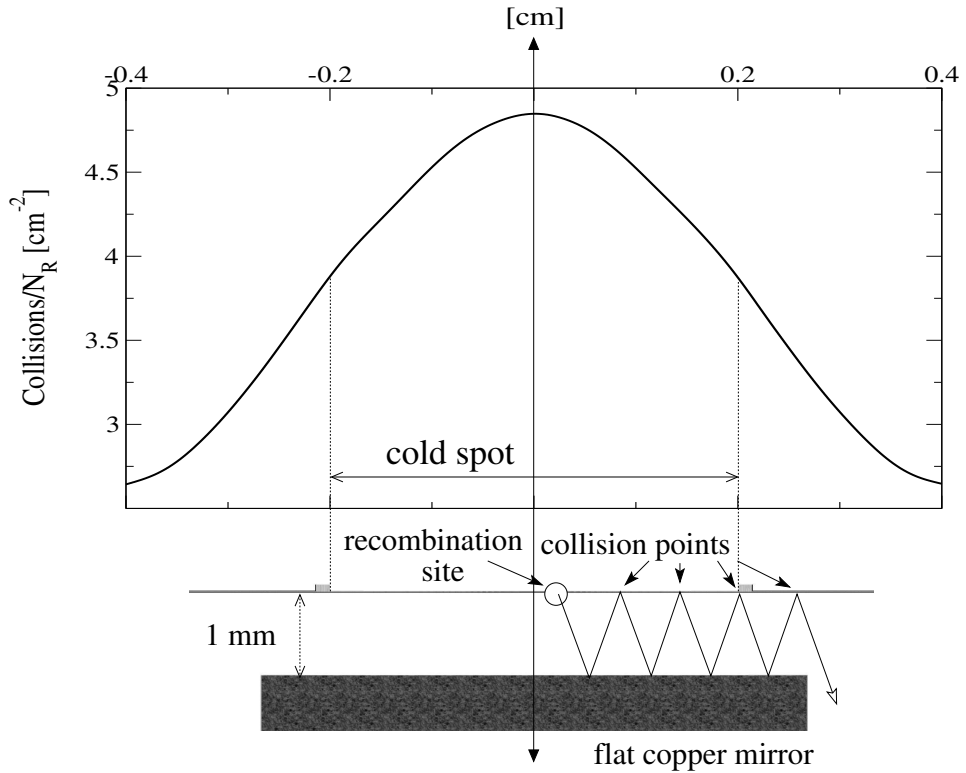
Figure 15: Scheme of the CS overheating in SCII and a calculated flux of H_2^* molecules bouncing between the CS and the flat mirror divided by the number of recombination events.

such that the asymmetry depended on the direction of the current in the coil.

As illustrated in fig. 14 we studied also the dependence of the line shape on the surface density. At small densities, $\sigma < 3 \times 10^{12}$ cm^{-2}, the linewidth is a linear function of σ but when the surface density exceeds 3×10^{12} cm^{-2} the surface line starts to broaden sharply. At the same time it becomes asymmetric, resembling the middle spectrum in fig. 13. The inhomogeneity of the dipolar field discussed above or changes in the intrinsic line shape can be reasons for the observed asymmetry. In principle one should be able to eliminate the field inhomogeneity effect by applying a gradient opposite to $\alpha_d\sigma(r)$. In fact we managed to make the line more symmetric and narrower by applying a radial gradient $\frac{\partial B_z}{\partial r}$ which increases towards the edge of the spot (as shown in the lower most example in fig. 13). Such a dipolar field means that $\sigma(r)$ is smallest at the center and increases towards the edge of the CS. A reasonable explanation for the smaller surface density in the center could be an extra heat flux to this region of the CS.

The idea behind an open-geometry resonator was that the flux of highly excited molecules

(H_2^*), which form on the cold spot, can easily escape and relax to the ground state in other parts of the cell. Most of the molecules impinging on the helium film are reflected since they are estimated to need approximately 150 surface collisions to release half of their rotational and vibrational energy [63]. In SCII the flat mirror of the resonator is at a distance of only 1 mm below the CS surface. Molecules scattering from the flat mirror increase the number of H_2^* hitting the center of the CS. To estimate the heat flux due to the bouncing H_2^*, the molecules were assumed to have random flight directions and recombination sites on the CS. Only elastic reflections were considered during the flight between the CS and the flat mirror as illustrated in fig. 15. After reaching the edge of the flat mirror the molecules were considered to escape. A numerical solution gives a parabolic profile of the H_2^* flux at the center of the CS. The flux is $4.8 A_{CS}\dot{\sigma}$ cm^{-2} at the center and 1.6 times lower at the edge of the CS. The average excitation energy of H_2^* released in a single wall collision is about 170 K$\times k_B$. This causes a heating power flux of about 250 K $\times k_B \dot{\sigma}$ cm^{-2}, comparable to the direct recombination heating of the surface, and it can hereby significantly alter the surface density profile. To reduce the heating of bouncing molecules, we modified the resonator of SCII by increasing the gap between the CS and the flat mirror. The preliminary results showed that this removed the sudden line broadening effect. The modification also allowed us to increase the surface density by a factor of 1.5 to 5.5×10^{12} cm^{-2} at which point a linewidth of about 0.3 G was measured.

3.1.3 Intrinsic broadening due to interatomic collisions

The intrinsic broadening of the magnetic resonance signal results from a transition between two spin states which are not sharply defined and have a finite relaxation time. In this work the intrinsic line shape f_i is defined as a line shape detected with a monochromatic mm-wave source in a uniform magnetic field and density. The intrinsic ESR linewidth for H↓⇊ surface atoms differs from that of atoms in the bulk. This is because the collisions of atoms, which perturb the resonance frequency of a free atom, are about 10^5 times more frequent on the surface than in the bulk.

One of the reasons for the broadening of the resonance line is the interatomic magnetic dipole interaction discussed in ref. [30]. In a random distribution of motionless atoms this interaction leads to a Gaussian line shape because each atom feels a different dipolar field and, accordingly, the spins will resonate at different frequencies. However, in a fluid or gas the atoms are in constant motion and each spin will sample over many different dipolar field values. If the motion is fast enough, this averaging compensates the dipolar line broadening and gives a line shape close to Lorentzian [84]. Our H↓⇊ sample can be modelled with hard spheres of radius $a = 0.36$ nm moving on a surface perpendicular to the polarizing field. The change of the resonance frequency, $\Delta\omega(t)$, due to the dipolar field during a head-on
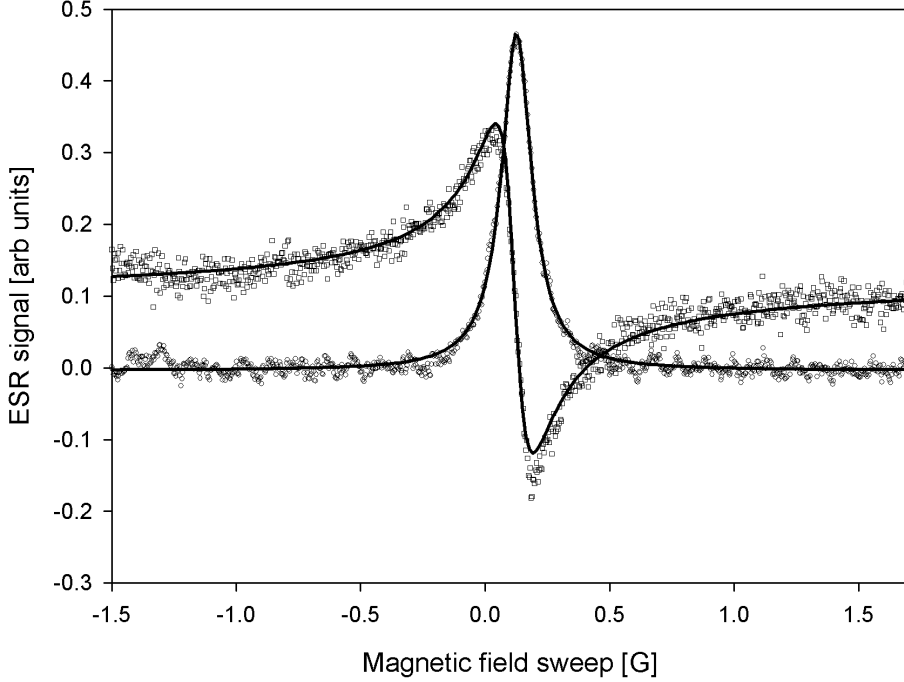
Figure 16: Absorption and dispersion spectra measured for surface atoms at $\sigma \approx 1.5 \times 10^{12}$ cm^{-2}. The solid lines are Lorentzian line shape fits to the data.

collision is given by $\frac{\mu_0}{4\pi}\frac{3}{4}\hbar\gamma_e^2/r(t)^3$ [85], where $r(t)$ is the distance between the spheres. During the collision the spin will precess an additional phase angle $\Delta\phi$ given by

$$\Delta\phi = 2\int_{-\infty}^{\frac{a}{v}} \Delta\omega(t)dt = -\frac{\mu_0}{4\pi}\frac{3\hbar\gamma_e^2}{4v_{2D}a^2}, \qquad (27)$$

where $v_{2D} = \sqrt{\pi k_B T/m}$ is the 2D relative thermal velocity of atoms. As $\Delta\phi$ is always negative, the net phase accumulates according to the atomic collision rate $\tau_c^{-1} \approx (a\sigma v_{2D})$. On the average, this shifts the resonance frequency of the spin by $\Delta\phi\tau_c^{-1}$, which is temperature independent and close to the dipolar shift in eq. (2). The net phase, making random walk steps of $\Delta\phi$, spreads a radian during the time T_2^{dip} according to the relation

$$\frac{1}{T_2^{dip}} = \frac{(\Delta\phi)^2}{\tau_c} = 8.0 \times 10^{-8}\frac{\sigma}{\sqrt{T_\sigma}} \text{ cm}^2\text{K}^{1/2}\text{s}^{-1}. \qquad (28)$$

The period T_2^{dip} is the transversal dipolar relaxation time of the spins, which gives the linewidth $2(\gamma_e T_2^{dip})^{-1} \approx 30$ mG at 100 mK and $\sigma = 10^{12}$ cm^{-2}. Then the line shape should

be Lorentzian since the condition for motional narrowing, $\Delta\omega\tau_c \approx \Delta\phi \ll 1$ [84], is satisfied throughout the whole experimental temperature range.

Spectral lines can be broadened also by the finite lifetime of the spin states. This is described by the longitudinal $\mathcal{T}_1$ relaxation, which results in a nonsecular or lifetime broadening proportional to $(2\mathcal{T}_1)^{-1}$ [68]. The lifetime of the spin states can be shortened by spontaneous emission, desorption, recombination and relaxation. In the experimental conditions of this work recombination is the fastest of these processes. The recombination time τ_{rec} is estimated from the $b-c$ recombination cross length $l_{bc} = 0.04 \times T$ nm/K [53]. Then, according to the uncertainty principle

$$\frac{1}{\mathcal{T}_1^{rec}} \approx \frac{1}{\tau_{rec}} = l_{bc}v_{2D}\sigma = 6.4 \times 10^{-5}T_\sigma^{3/2}\sigma \text{ cm}^2\text{K}^{-3/2}\text{s}^{-1}, \tag{29}$$

which yields a linewidth of about four times larger than the dipolar broadening.

The overall linewidth is given by $\mathcal{T}_2^{-1} \approx 1/\mathcal{T}_2^{dip} + 1/2\mathcal{T}_1^{rec}$ [68], where both terms are proportional to the surface density but have different temperature dependencies. As can be seen from fig. 14, for small densities the linewidth is indeed proportional to σ. The proportionality coefficient extracted from the fit to the data is of the order of $\mathcal{T}_2^{-1}$ as estimated above. The temperature dependence of the linewidth could not be clarified in the experiments. Narrower lines were observed at lower temperatures, indicating that the contribution of the $1/2\mathcal{T}_1^{rec}$ term is dominant. However, a contribution of the density inhomogeneity to this observation could not be ruled out completely. To unravel the sources of line broadening one needs further experiments where the instrumental linewidth is narrower and the temperature range wider.

3.2 Determination of surface gas temperature

In order to find out the degree of 2D quantum degeneracy ϖ_2 reached in the experiments one needs to know the temperature T_σ of the adsorbed H gas. Understandably there is no direct means to measure T_σ, but it can be extracted from the bulk and surface gas densities using the adsorption isotherm eq. (3). This method is described in ref. [P2] for the data obtained in the sample cell version SCI. Here we present a similar result for data measured at higher cell temperatures T_{sc} with SCII. Fig. 17 shows σ as a function of n measured at different T_{liq}. When T_{liq} is high enough, T_σ and T_b are constant because the recombination overheating is small. Then the surface density increases linearly with n, as expected according to eq. (3), with the slope proportional to $\Lambda(T_b/T_\sigma)^{3/2}\exp(E_a/T_\sigma)$. Using the adsorption energy $E_a/k_B = 1.14(1)$ K [53] we calculated from the slope the surface gas temperature T_σ. It deviated less than 1 mK from the coolant temperature T_{liq}. This difference is within the accuracy of our thermometry. To our knowledge this is the first experimental check of

41
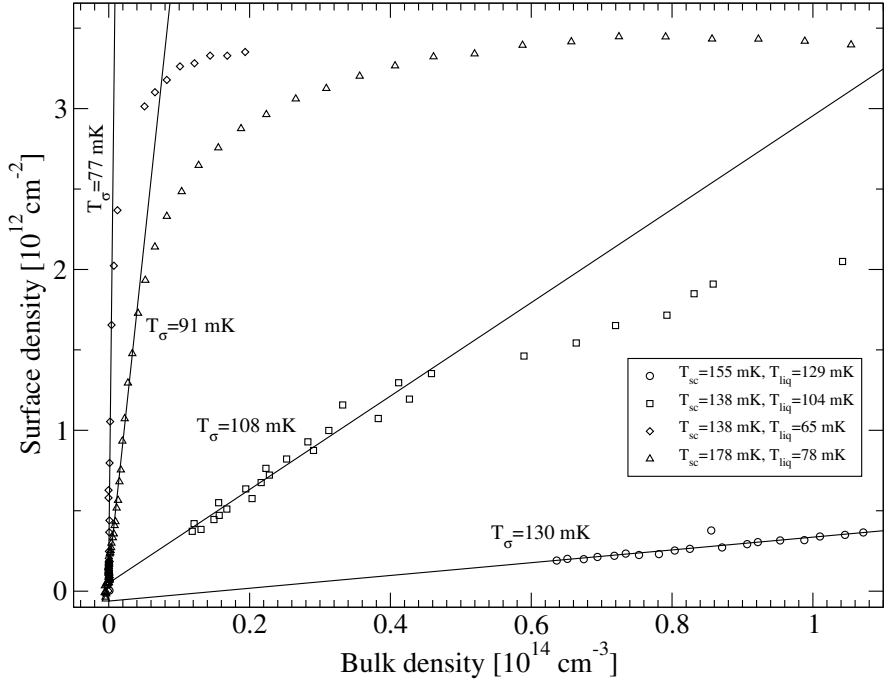
Figure 17: Measured surface density plotted as a function of bulk density for several decays at different T_{liq} and T_{sc} in SCII. The surface temperature T_σ is extracted by fitting the adsorption isotherm to the linear part of the data (solid lines).

the adsorption isotherm in the case of different bulk and surface gas temperatures. Due to a much smaller temperature difference $T_b - T_\sigma$ this was not possible in experiments with SCI. At high σ the quantum statistics and the interatomic interactions have to be taken into account when the surface gas temperature is extracted (eq. (4)). The observed levelling of σ with increasing n in fig. 17 points to overheating of the surface gas which begins at a smaller n the lower T_{liq} is.

3.3 Measurement of surface three-body recombination rate

One of the key parameters in the thermal compression of 2D H↓↕ is the surface three-body recombination rate constant L_3^s. Together with the cooling power via the ripplon-phonon contact, it sets a limit to the highest attainable surface density. In this work L_3^s has been extracted from independent measurements of the recombination power and surface density. From the data obtained with SCI we were able to make a rough estimate of L_3^s, although the contribution of the CS was barely distinguishable from the one-body relaxation. Due to the larger spot size in SCII the CS contribution to the recombination power was clearly visible and we could make a quantitative study of surface three-body recombination [P6].
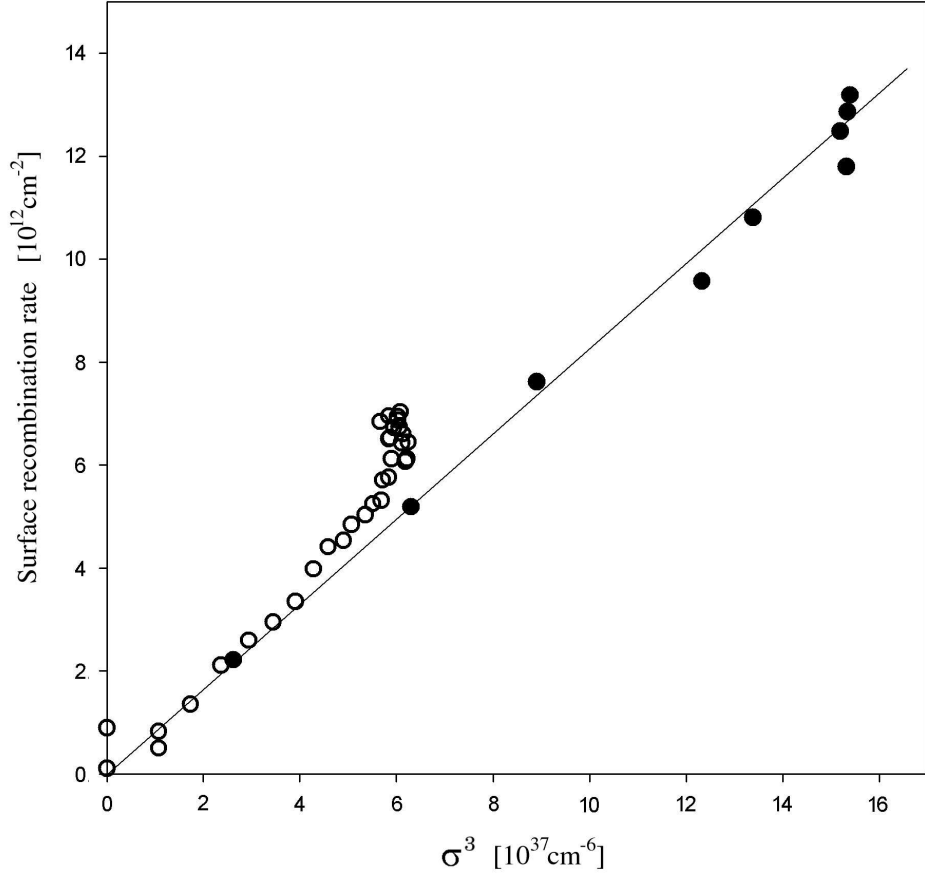
Figure 18: Measurement of the surface three-body recombination rate constant at $T_b = 178$ mK. Open symbols are before and closed symbols after the modification of SCII. Dashed line is a fit to the closed data points.

For a highly polarized sample the decay rate can be approximated by the decay of the bulk density as a sum of three-body recombination on the CS and one-body relaxation on the SC walls (eq. (7)). The recombination power P_{rec} released in the SC is then given by

$$P_{rec} \approx DV_h G^e n + \frac{D}{2} A_{cs} L_3^s \sigma^3, \tag{30}$$

where $A_{cs} = 0.3$ cm^2 is the area of the CS. By changing T_{liq} the three-body recombination term in eq. (30) can be easily varied in a wide range without influencing the one-body relaxation term. The contribution of the CS to the recombination power is obtained by subtracting the one-body relaxation decay measured for a high T_{liq} from the decay measured at the lowest T_{liq} when σ is highest. The result is shown in fig. 18 where the difference

$2(P_{rec} - DV_h G^e n)/D$ is plotted as a function of the third power of the surface density. The open and closed symbols refer to measurements, respectively, before and after the modifications of the sample cell SCII.

The upward trend of the open-symbol data for $\sigma \gtrsim 3 \times 10^{12}$ cm^{-2} in fig. 18 begins at the same surface density where the ESR line shape starts to become asymmetric. This feature may be accounted for by the overheating of the CS center by excited H$_2$ molecules bouncing from the flat mirror, as discussed in section 3.1.2. The ESR signal originates from atoms near the CS center only. In the case of the overheating the detected σ is therefore lower than the average σ on the CS and the corresponding data points in fig. 18 are shifted towards lower σ. The value $L_3^s = 2(1) \times 10^{25}$ cm^{4}s^{-1} [P6] is extracted from the data points which follow a linear dependence in fig. 18. The data measured after the cell modifications is entirely linear and up to the highest densities consistent with the above-mentioned L_3^s value. The results obtained for L_3^s in different experimental runs of the present work at temperatures between 85 and 130 mK are reproducible but approximately 10 times smaller than the previously reported values (cp. e.g. refs. [51, 52, 79]). A possible explanation for this large deviation could be the indirect determination of the surface density and recombination power in earlier measurements. This important issue is discussed in more detail in papers [P2] and [P6].

Theoretical studies of the surface three-body recombination were performed by Kagan *et al.* [36] and de Goey *et al.* [62]. Due to the absence of exchange interaction in mutual collisions of *b*-state atoms the dipole mechanism is the only efficient recombination process which was discussed by both of these theory groups. Kagan *et al.* used a simplified approach where the surface rate constant was calculated from the bulk rate constant by scaling the latter to the surface using the relation $L_3^s \approx L_3^b/l_d^2$. De Goey *et al.* took the delocalization more accurately into account, and obtained $L_3^s = 1.3 \times 10^{-25}$ cm^{4}s^{-1} at 4.6 T which is more than an order of magnitude smaller than the value reported by Kagan *et al.* [36]. Compared to our experimental result de Goey's calculation is within the error bar, which brings down the long-term discrepancy between theoretical and experimental values of L_3^s.

3.4   Limits of thermal compression

In this work the highest surface density observed was about 5.5×10^{12} cm^{-2} at $T_\sigma \approx 110$ mK, corresponding to the 2D phase-space density $\varpi_2 \approx 1.6$. The dense surface gas was overheated well above the coolant temperature and σ was almost independent of the bulk gas density as shown in fig. 17. The main source of heat was caused directly by recombination of the surface gas. Neglecting other sources of heat except the three-body surface recombination, a simple equation for the maximum quantum degeneracy ϖ_2 on the CS can be derived. The recombination heat absorbed by the surface of the cold spot is given by

$$P_{3b} = (f + (1-f)\frac{A_{cs}}{A_c})\frac{D}{2}L_3^s\sigma^3, \tag{31}$$

where A_c is the area of the sample cell, and f is the fraction of the heat dumped directly to the cold spot surface ($f \leq 2$ % [26, 63, 65]). The efficiency with which this heat can be removed is defined by the ripplon-phonon thermal contact (eq. (5)). Setting $P_{3b} = P_{rp}$ we get an estimate of the highest achievable quantum degeneracy as

$$\varpi_2 \equiv \sigma\Lambda^2 = \frac{2\pi\hbar^2}{mk_B}\sqrt[3]{\frac{2G_{rp}}{DL_3(f+(1-f)\frac{A_{CS}}{A_C})}}T_\sigma^{\frac{11}{9}} \approx 22T_\sigma^{\frac{11}{9}}. \tag{32}$$

In fig. 19 we present the highest ϖ_2 data obtained in SCII together with plots of the adsorption isotherm at several surface temperatures. Two sets of data are plotted, one taken before and the other after the improvement of the H_2^* escape from the CS, as described in section 3.1.2. The result of the improvement can be clearly seen as a factor of 1.5 increase in the surface density. Eq. (32), together with the adsorption isotherm (3), implicitly defines the maximum surface density $\sigma(n)$, which can be reached for a given bulk density n and temperature T_b. For $T_b = 178$ mK we plot $\sigma(n)$ in fig. 19 as the dotted line. The dashed line marks the condition of quasi-condensate formation $\varpi_2 = 3$ [20]. We include an abrupt change of the interactions in 2D gas, taken into account by the two-body correlator g_2 in eq. (4), which leads to an increase of σ by a factor of two in the quasi-condensate [46].

Eq. (5) predicts that in order to increase ϖ_2 one has to use higher T_σ. One can estimate that the condition $\varpi_2 \approx 3$ required for quasi-condensate formation can be reached at $T_\sigma \approx$ 200 mK and $n \approx 10^{17}$ cm^{-3}, found as a crossing of the dashed and dotted lines in fig. 19. The use of such a high bulk density would increase the heating of the surface due to the thermal accommodation,

$$P_{acc} = \frac{nv_3s}{4}2k_B(T_b - T_\sigma). \tag{33}$$

The heating P_{acc} becomes comparable with the surface three-body recombination heating if the temperature difference exceeds 100 mK at $n = 6 \times 10^{16}$ cm^{-3}. Therefore, a further increase of n does not help to reach a higher degeneracy of the surface gas. On the other hand, from the experimental data of fig. 19 it is evident that only a twofold increase of σ would be needed. Some increase of ϖ_2 may be possible by a further improvement of the escape of H_2^*. This can be done by making the cell more open by using e.g. a coarse grid as a mirror below the spot. Another way to work is to increase the adsorption energy. This can be done by utilizing a thin unsaturated helium film [49] at the CS. The thinner film will possibly reduce the value of L_3^s [P6] and increase the ripplon-phonon thermal contact. Making a superfluid helium film locally thinner is, however, a difficult technical problem
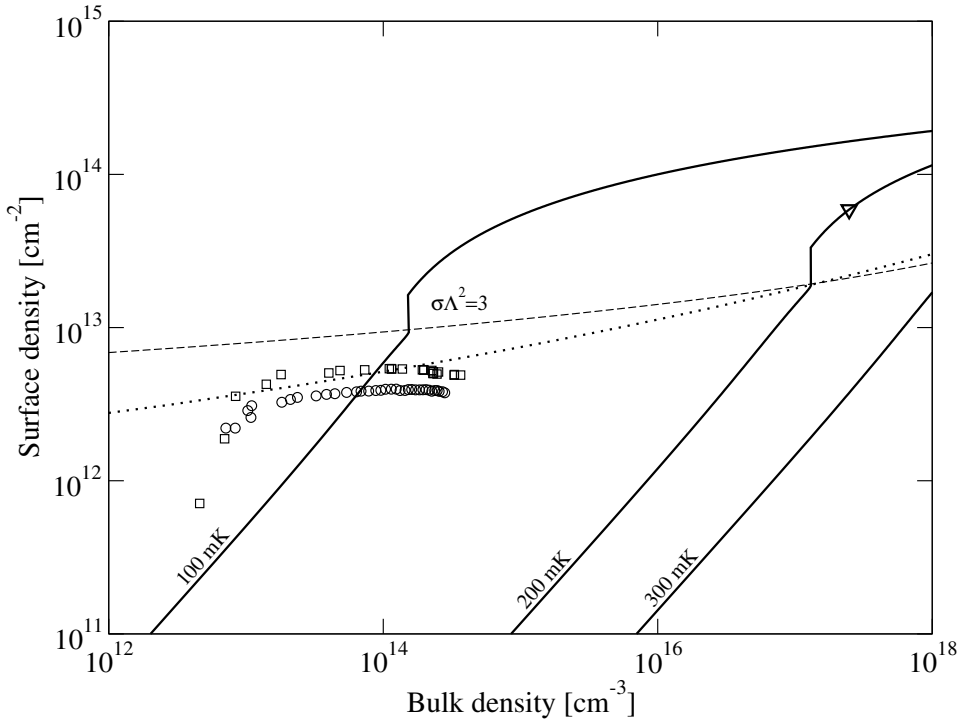
Figure 19: Thick solid lines: Calculated isotherms of the surface gas. Dashed line: Quasi-condensate formation at $\sigma\Lambda^2 = 3$. Dotted line: Values calculated from eq. (32). Experimental data (○) and (□) are obtained in SCII at $T_{liq} = 67$ mK and $T_C = 178$ mK. The latter data (□) is measured after the sample cell modification. The point ($\triangledown$) corresponds to 2D quantum degeneracy achieved in ref. [20] with magnetic compression.

and one for which we do not know a ready solution.

4 Conclusions

We have investigated experimentally the properties of electron- and nuclear-polarized atomic hydrogen H↓⇂ gas adsorbed on the surface of superfluid ^{4}He films at temperatures from 80 mK to 140 mK. To minimize surface recombination the surface density was increased, up to 5.5×10^{12} cm^{-2}, in a small area only. The temperature difference between this small "cold spot" and the sample cell compressed the two-dimensional gas to about 100 times larger surface density on the spot than on the cell walls. Both bulk and surface atoms were detected with a cryogenic ESR spectrometer operated at 129 GHz and connected to a Fabry-Perot resonator.

The surface line shape is shown to be very sensitive to the ESR excitation power. The interatomic dipolar interactions shift the resonance frequency of the surface-confined atoms

from that of the 3D gas. An excitation power level as low as a nanowatt is found to be sufficient to disturb the equilibrium surface density and the intrinsic dipolar field of the surface atoms, resulting in a nonlinear response of the ESR signal which may be called "ESR instability". This effect distorts the ESR lines to almost triangular shape and causes a hysteresis of the line position. When the excitation power is reduced, the line shape becomes more symmetric and depends on the magnitude and distribution of the surface density. The observed line broadening which includes the residual line broadening due to the spectrometer agrees roughly with the estimates of a fluctuating intrinsic dipolar field and recombination.

The bulk and surface densities were extracted from the ESR spectra and, together with the measurement of the recombination heat, provided a direct determination of the surface three-body recombination rate constant L_3^s. This first independent measurement of recombination power and surface density yielded $L_3^s = 2(1) \times 10^{-25}$ cm^{-4}s^{-1}, which is an order of magnitude smaller than in previous experiments. The new result settles some lingering discrepancies between theoretical and experimental values. The smaller value is also encouraging for further compression experiments.

Two significant heat sources of the surface gas were identified and removed, the impurity relaxation and the relaxation of excited H_2 molecules in the compression region. The former was eliminated by coating the sample cell walls with epoxy, polymer foils, and a solid H_2 layer. By making the geometry more open the bouncing excited molecules could easily escape from the region of the cold spot. After these measures the surface gas density could be increased by a factor of 1.5, and a maximum density of about 5.5×10^{12} cm^{-2} was reached, corresponding to a two-dimensional degree of 1.6 in quantum degeneracy.

References

[1] E. C. Zachmanoglou and W. T. Thoe, *Introduction to Partial Differential Equations with Applications* (Dover Publications, Inc., 1986).

[2] K. B. Davis, M. O. Mewes, M. R. Andrews, N. J. Vandruten, D. S. Durfee, D. M. Kurn, and W. Ketterle, Phys. Rev. Lett. **75**, 3969 (1995).

[3] M. H. Anderson, J. R. Ensher, M. R. Matthews, C. E. Wieman, and E. A. Cornell, Science **269**, 198 (1995).

[4] N. D. Mermin, Phys. Rev. **176**, 250 (1968).

[5] N. D. Mermin and H. Wagner, Phys. Rev. Lett **22**, 1133 (1966).

[6] P. C. Hohenberg, Phys. Rev. **158**, 383 (1967).

[7] V. L. Berezinskii, Sov. Phys. JETP **32**, 493 (1971).

[8] J. M. Kosterlitz and D. J. Thouless, *Two-dimensional physics*, in *Progress in low temperature physics*, edited by D. F. Brewer (North-Holland, 1978), vol. VIIb, p. 374.

[9] M. Bijlsma, Quantum degeneracy in a Bose gas, Ph.D. thesis, Eindhoven University of Technology, Netherlands (1997).

[10] D. J. Bishop and J. D. Reppy, Phys. Rev. Lett **40**, 1727 (1978).

[11] V. N. Popov, *Functional integrals in quantum field theory and statistical physics* (Reidel, Dordrecht, 1983).

[12] D. S. Petrov, D. M. Gangardt, and G. V. Shlyapnikov, *Low-dimensional trapped gases*, in *Journal de Physique IV*, edited by L. Pricoupenko, H. Perrin, and M. Olshanii (EDP Sciences, 2004), vol. 116, p. 3.

[13] M. Bijlsma and H. T. C. Stoof, Phys. Rev. E **47**, 939 (1993).

[14] J. O. Andersen, U. Al Khawaja, and H. T. C. Stoof, Phys. Rev. Lett **88**, 070407 (2002).

[15] U. Al Khawaja, J. O. Andersen, N. P. Proukakis, and H. T. C. Stoof, Phys. Rev. A **66**, 013615 (2002).

[16] Yu. Kagan, V. A. Kashurnikov, A. V. Krasavin, N. V. Prokof'ev, and B. V. Svistunov, Phys. Rev. A **61**, 043608 (2000).

[17] N. Prokofev and B. Svistunov, Phys. Rev. A **66**, 043608 (2002).

[18] I. F. Silvera and J. T. M. Walraven, Phys. Rev. Lett **44**, 164 (1980).

[19] D. G. Fried, T. C. Killian, L. Willmann, D. Landhuis, S. C. Moss, D. Kleppner, and T. J. Greytak, Phys. Rev. Lett **81**, 3811 (1998).

[20] A. I. Safonov, S. A. Vasilyev, I. S. Yasnikov, I. I. Lukashevich, and S. Jaakkola, Phys. Rev. Lett **81**, 4545 (1998).

[21] M. Greiner, I. Bloch, O. Mandel, T. W. Hänsch, and T. Esslinger, Appl. Phys. B **73**, 769 (2001).

[22] J. M. Görlitz, J. M. Vogels, A. E. Leanhardt, C. Raman, T. L. Gustavson, J. R. Abo-Shaeer, A. P. Chikkatur, S. Gupta, S. Inouye, T. Rosenband, and W. Ketterle, Phys. Rev. Lett **87**, 130402 (2001).

[23] M. Hammes, D. Rychtarik, B. Enseger, H.-C. Nägerl, and R. Grimm, Phys. Rev. Lett **90**, 173001 (2003).

[24] S. Dettmer, D. Hellweg, P. Ryytty, J. J. Arlt, W. Ertmer, K. Sengstock, D. S. Petrov, G. V. Shlyapnikov, H. Kreutzmann, L. Santos, and M. Lewenstein, Phys. Rev. Lett **87**, 160406 (2001).

[25] S. Stock, Z. Hadzibabic, B. Battelier, M. Cheneau, and J. Dalibard, Phys. Rev. Lett **95**, 190403 (2005).

[26] A. Matsubara, T. Arai, S. Hotta, J. S. Korhonen, T. Suzuki, A. Masaike, J. T. M. Walraven, T. Mizusaki, and A. Hirai, Physica B **194**, 899 (1994).

[27] S. Gupta, Z. Hadzibabic, M. W. Zwierlein, C. A. Stan, K. Dieckmann, C. H. Schunck, E. G. M. Van Kempen, B. J. Verhaar, and W. Ketterle, Science **300**, 1723 (2003).

[28] D. M. Harber, H. J. Lewandowski, J. M. Mcguirk, and E. A. Cornell, Phys. Rev. A **66**, 053616 (2002).

[29] M. W. Zwierlein, Z. Hadzibabic, S. Gupta, and W. Ketterle, Phys. Rev. Lett **91**, 250404 (2003).

[30] I. Shinkoda and W. N. Hardy, J. Low Temp. Phys. **85**, 99 (1991).

[31] W. Kolos and L. Wolniewicz, J. Chem. Phys. **43**, 2429 (1965).

[32] W. Kolos and L. Wolniewicz, Chem. Phys. Lett. **24**, 457 (1974).

[33] C. E. Hecht, Physica **25**, 1159 (1959).

[34] I. F. Silvera and J. T. M. Walraven, *Spin-polarized atomic hydrogen*, in *Progress in Low Temperature Physics*, edited by D. F. Brewer (North-Holland, Amsterdam, 1986), vol. X, p. 139.

[35] Y. P. Zhang, C. H. Cheng, J. T. Kim, J. Stanojevic, and E. E. Eyler, Phys. Rev. Lett **92**, 203003 (2004).

[36] Yu. Kagan, I. A. Vartanyants, and G. V. Shlyapnikov, Sov. Phys. JETP **54**, 590 (1981).

[37] J. M. Greben, A. W. Thomas, and A. J. Berlinsky, Can. J. Phys. **59**, 945 (1981).

[38] L. P. H. De Goey, J. P. J. Driessen, Verhaar B. J., and J. T. M. Walraven, Phys. Rev. Lett **53**, 1919 (1984).

[39] M. W. Reynolds, I. Shinkoda, W. N. Hardy, A. J. Berlinsky, F. Bridges, and B. W. Statt, Phys. Rev. B **31**, 7503 (1985).

[40] R. A. Guyer and M. D. Miller, Phys. Rev. Lett **42**, 1754 (1979).

[41] I. B. Mantz and D. O. Edwards, Phys. Rev. B **20**, 4518 (1979).

[42] D. O. Edwards and W. F. Saam, *The free surface of liquid helium*, in *Progress in Low Temperature Physics*, edited by D. F. Brewer (North-Holland, Amsterdam, 1978), vol. VII A, p. 283.

[43] J. T. M. Walraven, *Atomic hydrogen and liquid helium surfaces*, in *Fundamental systems in quantum optics*, edited by J. Dalibard, J. M. Raimond, and J. Zinn-Justin (Elsevier Science Publishers, Amsterdam, 1992), p. 487.

[44] H. Gauck, M. Hartl, D. Schneble, H. Schnitzler, T. Pfau, and J. Mlynek, Phys. Rev. Lett **81**, 5298 (1998).

[45] E. A. Hinds, M. G. Boshier, and I. G. Hughes, Phys. Rev. Lett **80**, 645 (1998).

[46] B. V. Svistunov, T. M. Hijmans, G. V. Shlyapnikov, and J. T. M. Walraven, Phys. Rev. B **43**, 13412 (1991).

[47] J. J. Berkhout and J. T. M. Walraven, Phys. Rev. B **47**, 8886 (1993).

[48] I. A. Yu, J. M. Doyle, J. C. Sandberg, C. L. Cesar, D. Kleppner, and T. J. Greytak, Phys. Rev. Lett. **71**, 1589 (1993).

[49] H. P. Godfried, E. R. Eliel, J. G. Brisson, J. D. Gillaspy, C. Mallardeau, J. C. Mester, and I. F. Silvera, Phys. Rev. Lett **55**, 1311 (1985).

[50] M. Morrow, R. Jochemsen, A. J. Berlinsky, and W. N. Hardy, Phys. Rev. Lett **47**, 455 (1981).

[51] D. A. Bell, H. F. Hess, G. P. Kochanski, S. Buchman, L. Pollack, Y. M. Xiao, D. Kleppner, and T. J. Greytak, Phys. Rev. B **34**, 7670 (1986).

[52] R. Sprik, J. T. M. Walraven, G. H. Van Yperen, and I. F. Silvera, Phys. Rev. B **34**, 6172 (1986).

[53] A. I. Safonov, S. A. Vasiliev, A. A. Kharitonov, S. T. Boldarev, I. I. Lukashevich, and S. Jaakkola, Phys. Rev. Lett **86**, 3356 (2001).

[54] D. S. Zimmerman and A. J. Berlinsky, Can. J. Phys. **62**, 590 (1984).

[55] M. W. Reynolds, I. D. Setija, and G. V. Shlyapnikov, Phys. Rev. B **46**, 575 (1992).

[56] O. V. Lounasmaa, *Experimental principles and methods below 1 K* (Academic Press, 1974).

[57] M. D. Lee, S. A. Morgan, M. J. Davis, and K. Burnett, Phys. Rev. A **65**, 043617 (2002).

[58] D. S. Petrov and G. V. Shlyapnikov, Phys. Rev. A **64**, 012706 (2001).

[59] M. J. Jamieson, A. Dalgarno, and J. N. Yukich, Phys. Rev. A **46**, 6956 (1992).

[60] Yu. Kagan, B. V. Svistunov, and G. V. Shlyapnikov, Sov. Phys. JETP **66**, 314 (1987).

[61] D. S. Petrov, M. Holzmann, and G. V. Shlyapnikov, Phys. Rev. Lett **84**, 2551 (2000).

[62] L. P. H. De Goey, H. T. C. Stoof, J. M. V. A. Koelman, B. J. Verhaar, and J. T. M. Walraven, Phys. Rev. B **38**, 11500 (1988).

[63] S. A. Vasiliev, E. Tjukanoff, M. Mertig, A. Ya. Katunin, and S. Jaakkola, Europhys. Lett. **24**, 223 (1993).

[64] A. Matsubara, T. Arai, S. Hotta, J. S. Korhonen, T. Suzuki, A. Masaike, J. T. M. Walraven, T. Mizusaki, and A. Hirai, Physica B **194-196**, 899 (1994).

[65] E. S. Meyer, Z. Zhao, J. C. Mester, and I. F. Silvera, Phys. Rev. B **50**, 9339 (1994).

[66] E. A. Burt, R. W. Ghrist, C. J. Myatt, M. J. Holland, E. A. Cornell, and C. E. Wieman, Phys. Rev. Lett **79**, 337 (1997).

[67] Yu. Kagan, B. V. Svistunov, and G. V. Shlyapnikov, JETP Lett. **42**, 208 (1985).

[68] C. P. Slichter, *Principles of Magnetic Resonance* (Springer-Verlag, Heidelberg, 1992), third edn.

[69] B. W. Statt, W. N. Hardy, A. J. Berlinsky, and E. Klein, J. Low Temp. Phys. **61**, 471 (1985).

[70] G. H. Van Yperen, J. T. M. Walraven, and I. F. Silvera, Phys. Rev. B **30**, 2386 (1984).

[71] M. Mertig, E. Tjukanov, S. A. Vasilyev, A. Ya. Katunin, and S. Jaakkola, J. Low Temp. Phys. **100**, 45 (1995).

[72] B. Yurke, D. Igner, E. Smith, B. Johnson, J. Denker, C. Hammel, D. Lee, and J. Freed, J. Phys-Paris (Colloq.) **C7**, 177 (1980).

[73] N. Bloembergen and R. V. Pound, Phys. Rev. **95**, 8 (1954).

[74] C. P. Poole, *Electron Spin Resonance* (John Wiley and Sons, 1967).

[75] H. A. Haus, *Waves and fields in optoelectronics* (Prentise-Hall Inc., 1984), first edn.

[76] S. A. Vasiliev, A. Ya. Katunin, A. I. Safonov, A. V. Frolov, and E. Tjukanoff, Appl. Magn. Reson. **3**, 1061 (1992).

[77] R. Van Roijen, J. J. Berkhout, B. Hebral, and J. T. M. Walraven, A cryogenic dissociator for atomic hydrogen (1989). Universiteit van Amsterdam, unpublished.

[78] H. Kogelnik and T. Li, Proc. IEEE **54**, 1312 (1966).

[79] H. F. Hess, D. A. Bell, G. P. Kochanski, D. Kleppner, and T. J. Greytak, Phys. Rev. Lett. **52**, 1520 (1984).

[80] B. W. Statt, A. J. Berlinsky, and W. N. Hardy, Phys. Rev. B **31**, 3169 (1985).

[81] R. Sprik, J. T. M. Walraven, G. H. Van Yperen, and I. F. Silvera, Phys. Rev. Lett **49**, 153 (1982).

[82] P. W. Anderson and H. Suhl, Phys. Rev. **100**, 1788 (1955).

[83] B. Lax and K. J. Button, *Microwave ferrites and ferrimagnets* (McGraw-Hill, 1962).

[84] R. Kubo, M. Toda, and N. Hashitsume, *Statistical physics II : Nonequilibrium statistical mechanics* (Springer-Verlag, 1985).

[85] C. P. Poole and H. A. Farach, *Relaxation in magnetic resonance* (Academic press, 1971).